The Developing Region of a Turbulent Coaxial Jet

by

Gilbert Milanovic

Department of Mechanical Engineering
McGill University
Montreal, Canada
December 2017

A thesis submitted to McGill University
in partial fulfillment of the requirements of the degree of
Master of Engineering

Abstract

Scalar mixing in the developing region of a turbulent coaxial jet was investigated experimentally. The primary objective of this work was to perform single scalar measurements at three downstream locations in a coaxial jet of water. The secondary objective was to determine radial positions within the jet structure where multi-scalar measurements should be made, as part of a bigger study involving multi-scalar mixing in turbulent flows.

Experiments were conducted in a momentum-driven, axisymmetric turbulent coaxial jet of water containing a passive scalar in the form of a fluorescent dye. Using planar laser-induced fluorescence (PLIF), planar scalar measurements were obtained at three downstream locations ($x/D_{in} = 2, 5$ and 10) from the jet exit. The Reynolds number of the inner (jet) flow was 6700, the Reynolds number of the outer (annular) flow was 5500, the Schmidt number was 2000, the jet area ratio was 2.54, the velocity ratio was 1, and the jet exit velocity profile was fully developed. Planar concentration measurements were also obtained at the same downstream locations for a simple jet, with a Reynolds number of 6700.

Radial profiles of the mean, root-mean-square (rms) and skewness of the concentration, as well as probability density functions, were computed and discussed. The results supported the established trend that higher mean velocity gradients lead to more mixing and faster jet development. The results also implied the possible presence of energetic coherent structures formed in the outer shear layer of the coaxial jet (between the outer flow and the ambient fluid).

The experimental conditions used during the coaxial jet tests are novel in the literature; in addition this work presents the first radial profiles of the skewness of the concentration in a coaxial jet. Furthermore, the first set of planar scalar measurements in a simple jet for downstream distances of $x/D_{in} < 5$ is also presented.

Résumé

Ce mémoire présente une étude expérimentale portant sur le mélange de scalaires dans la région en développement d'un jet coaxial turbulent. L'objectif principal de ce projet consistait à mesurer un scalaire à trois endroits en aval d'un jet d'eau coaxial. L'objectif secondaire était de déterminer les positions radiales de la structure du jet où des mesures multi-scalaires devraient être prises dans le cadre d'une plus grande étude concernant le mélange multi-scalaire dans les écoulements turbulents.

Les expériences ont été menées dans un jet d'eau coaxial turbulent axisymétrique contenant un scalaire passif sous forme de traceur fluorescent. Une technique de fluorescence induite au laser a été utilisée pour obtenir des mesures de scalaire à trois endroits en aval de la sortie du jet ($x/D_{in} = 2, 5$ et 10). Les nombres de Reynolds correspondant aux écoulements intérieur (jet) et extérieur (annulaire) s'élevaient respectivement à 6700 et 5500, le nombre de Schmidt était 2000, le rapport des surfaces du jet était 2.54, le rapport des vitesses était 1 et le profil de vitesse à la sortie du jet était pleinement développé. Afin de comparer les résultats obtenus, des mesures de scalaire aux 3 mêmes endroits en aval de la sortie du jet ont également été effectuées en se servant d'un jet simple dont le nombre de Reynolds équivalait 6700.

Les profils radiaux de la moyenne, la moyenne quadratique et le coefficient de dissymétrie de la concentration, ainsi que la densité de probabilité des fluctuations de concentration, ont été calculés et discutés. Les résultats sont en accord avec le paradigme qui stipule que les gradients de vitesse moyennes élevés produisent un mélange de scalaires plus intense et, par conséquence, accélèrent le

développement du jet. Les résultats suggèrent également l'existence probable de structures turbulentes énergétiques formées dans la couche de cisaillement externe du jet coaxial (entre l'écoulement extérieur du jet et le fluide qui compose le milieu ambiant).

Ce travail présente les premières mesures de scalaire effectuées dans un jet simple pour les distances en aval de $x/D_{in} < 5$. De plus, les conditions expérimentales utilisées lors des tests impliquant le jet coaxial étaient jusqu'à maintenant inexistantes dans la littérature. Ce travail présente également les premiers profils radiaux du coefficient de dissymétrie dans un jet coaxial.

Acknowledgements

I would firstly like to thank my supervisors, Professor Laurent Mydlarski and Professor Susan Gaskin. They both provided me with great advice and guidance throughout the course of my studies. Specifically, I would like to thank Professor Mydlarski for his attention to detail and great mind, both of which have been personal source of inspiration. I would also like to thank Professor Gaskin for her grounded and unique approach to research and life, which has also influenced me for the better.

Furthermore, I am grateful for the financial support I received from the Fonds de recherche du Québec - Nature et technologie (FRQNT) and from the Faculty of Engineering. Their continued support helped me remain focused on the research task at hand.

My project would have not been possible without the extremely useful and generous help I received from John Bartczak and Alejandro Perez-Alvarado. John was essential in helping me build my various contraptions, while Alajandro provided countless insights and ultimately helped define the direction my project. I would also like to thank my colleagues, Stephen Camozzi, Aaron Manzali, Claudio Consuegra Martínez and Michel Samson, for their companionship, help and Thompson House evenings.

Finally, I'd like to thank my friends, family and girlfriend, Laura, for their continued love and support throughout this, at times stressful, endeavor.

Table of Contents

List of Figures

List of Tables

Nomenclature

A	cross-sectional area
$A_{o/i}$	area ratio for coaxial nozzle
$\mathcal{A}, \mathcal{B}$	constants pertaining to the calibration curve fits
C	instantaneous concentration
C_0	average jet exit concentration
C	general variable referring to the mean, rms or skewness of the concentration
c	fluctuating concentration
D	circular nozzle diameter
D_b	laser beam diameter
D_H	hydraulic diameter
$D_{o/i}$	diameter ratio for coaxial nozzle
$\mathcal{D}$	molecular diffusivity
d_0	waist diameter
f	focal length
I	fluorescence intensity
I_0	incident radiant power
L_c	core length
L_e	entrance length
L_d	dilution length
M	molar concentration
MW	molar weight
N	number of measurements
P	wetted perimeter
Pe	Péclet number $\left(\equiv \frac{U_0 \cdot D_H}{\mathcal{D}}\right)$
Pr	Prandlt number $(\equiv \nu/\alpha)$
r	jet radial coordinate
r_0	jet centerline
$r_{1/4}$	radial position where concentration has decayed by 25% of $C_{mean,CL}$
$r_{1/2}$	jet half-width, can pertain to velocity or concentration measurements
$r_{3/4}$	radial position where concentration has decayed by 75% of $C_{mean,CL}$
$r_{9/10}$	radial position where concentration has decayed by 90% of $C_{mean,CL}$
r_v	velocity ratio for coaxial jet
Re	Reynolds number $\left(\equiv \frac{U_0 \cdot D_H}{\nu}\right)$
Re_0	local Reynolds number based on $U_{mean,CL}$, $r_{1/2}$ and ν
S	density ratio for coaxial jet

S_C	skewness of the concentration
Sc	Schmidt number ($\equiv \nu/\mathcal{D}$)
T	instantaneous temperature
t'	fluctuating temperature
t	time
ΔT	instantaneous temperature excess
Δt	fluctuating temperature excess
U	instantaneous axial velocity
U_0	average jet exit velocity
u	fluctuating axial velocity
V	instantaneous radial velocity
v	fluctuating radial velocity
x	jet axial coordinate
x_0	virtual origin
Z	normalized concentration difference
Z_R	Rayleigh range

Greek Symbols

α	thermal diffusivity
β	molar absorptivity
b	path length of a cell
ε	dissipation rate of turbulent kinetic energy per unit mass
η	Kolmogorov lengthscale
η_B	Batchelor lengthscale
θ	jet azimuthal coordinate
λ	wavelength
μ	dynamics viscosity
ν	kinematic viscosity
ρ	density
σ	standard deviation
σ_{noise}	standard deviation pertaining to experimental noise
σ_{repeat}	standard deviation pertaining to experimental repeatability
σ_{signal}	standard deviation pertaining to the signal
$\sigma_{symmetry}$	standard deviation pertaining to jet axial symmetry
σ_T	total uncertainty pertaining to the mean, rms or skewness of the concentration
Φ_f	quantum efficiency

Superscripts and Symbols

$\langle\cdot\rangle$	denotes averaging in time
$\circ$	degree

Subscripts

CL	pertain to centerline quantity
i, in	pertains to inner nozzle/jet of a coaxial nozzle/jet
$mean$	pertains to mean quantity
o, out	pertains to outer nozzle/jet of a coaxial nozzle/jet
rms	pertains to root-mean square quantity

Acronyms

ID	inner diameter
LIF	laser-induced fluorescence
OD	outer diameter
PLIF	planar laser-induced fluorescence
PDF	probability density function
PMT	photomultiplier tube
SNR	signal to noise ratio

Chapter 1: Introduction

1.1 Background

Scalar mixing within turbulent flows is common in many industrial and environmental applications. For example, the concentration of a given pollutant in the atmosphere might be of interest for environmental and/or health concerns; similarly, the temperature in the ocean is useful for helping predict water currents and biological activity. In these examples, a single scalar is mixed in a background flow in a process referred to as single scalar mixing. Multi-scalar mixing processes, which involve 2 or more scalars, are also possible and have many practical applications. Combustion, for example, is a chemical reaction controlled in part by the simultaneous mixing of several reactants and products.

Of interest in the present work is scalar mixing within a turbulent coaxial jet. Such a jet such consists of a simple round jet surrounded by a concentric annular jet. Due to their fundamental nature as a relatively simple shear flow, coaxial jets are interesting to study from a purely analytical standpoint. However, they are also encountered in several practical applications. Many rockets, for example, use coaxial nozzles as fuel injectors, where the inner, slow-moving liquid oxidizer is fragmented and mixed with the outer, high momentum gaseous fuel in a process called *airblast atomization*. This fuel/oxidizer configuration can help reduce combustion chamber wall oxidation, while still providing adequate mixing. A coaxial jet is also formed at the exhaust of a high-bypass jet engine, which consists of an inner jet of hot exhaust

gases surrounded by an annular jet of bypassed air. By careful design, the noise generated by such an engine can be greatly reduced.

In both these examples, the flow development that occurs early in the downstream direction of the coaxial jet plays a crucial role in the overall dynamics of the process. In the case of coaxial fuel injectors, rapid and thorough mixing in the developing region ensures stable combustion and can help reduce the chamber size; in high-bypass jet engines, the coherent structures formed within the first 4 diameters downstream of the engine exit are responsible for most of the noise generation.

A large number of coaxial jet studies have focused on velocity measurements and, as a result, much progress has been made describing the early development of the velocity field and the coherent structure formation. Most importantly, it has been demonstrated that the velocity ratio (the ratio between the average outer and inner jet velocities) plays a significant role in the early downstream development; other variables, such as the Reynolds number and nozzle geometry have been systematically tested as well. Scalar measurements in coaxial jets, however, are less common. This fact, compounded by the number of possible experimental conditions pertaining to coaxial jet experiments, has resulted in several gaps in the literature. One such gap will be explored in this work. In addition, this work serves as an initial set of measurements (single scalar) to be used as a reference in future studies involving the simultaneous mixing of several scalars in coaxial jets.

A typical coaxial jet experiment performing scalar measurements can be defined by the following experimental conditions: the Reynolds number of the inner and outer jets, the Schmidt number, the area ratio, the velocity ratio and the nozzle exit velocity profile. Each of these parameters has been shown in past studies to impact the flow development to some extent and though they are described in more detail in Chapter 2, a brief overview is warranted here.

The Reynolds number is defined as: $Re \equiv \frac{U_0 \cdot D_H}{\nu}$, where U_0 is the average jet exit velocity, D_H is the jet hydraulic diameter $\left(D_H \equiv \frac{4A}{P}, \text{where } A \text{ is the cross} - \text{sectional area and } P \text{ is the wetted perimeter}\right)$ and ν is the kinematic viscosity of the fluid. This non-dimensional number represents the ratio of the inertial to viscous forces in the flow and it is the most useful measure in predicting the flow regime (laminar, transitional or turbulent). The Schmidt number is defined as: $\mathrm{Sc} \equiv \nu/\mathcal{D}$, where $\mathcal{D}$ is the molecular diffusivity of the scalar. Flows in water usually possess high Schmidt numbers (~ 1000), whereas flows in gas possess lower Schmidt numbers (~ 1). The area ratio ($A_{o/i}$) is the ratio of the outer to inner nozzle cross-sectional area and similarly, the velocity ratio (r_v) is the ratio of the average outer to inner jet exit velocity. Though the area ratio has been shown to have a relatively small effect on early coaxial mixing, the velocity ratio represents a very important parameter when considering the mixing dynamics in the developing region. For example, as the velocity ratio is increased from 1, faster mixing and jet development is achieved since shear between the flows is increased. Lastly, many exit velocity profiles are possible, the two most common being the top-hat and the fully developed pipe flow exit velocity profiles. The characteristics of the coherent structures formed early in the development of the coaxial jet, which are eventually propagated downstream, have been specifically linked to the exit velocity profile.

1.2 Objectives

This work investigates single scalar mixing early in the downstream flow development of a turbulent coaxial water jet issuing into a quiescent background. A passive scalar (fluorescent dye) was dissolved in the flow and its concentration was measured using planar laser-induced fluorescence.

The primary objective of this work is to perform single scalar measurement in the developing region of a coaxial jet of water with: $Re_{in} = 6700$, $Re_{out} = 5500$,

$Sc = 2000$, $A_{o/i} = 2.54$, $r_v = 1$ and a fully developed pipe flow exit velocity profile. To the writer's knowledge, scalar measurements in such a coaxial jet have yet to be performed. Furthermore, the nozzle geometry and flow conditions are relevant to the practical applications of coaxial jets (fuel injectors, high-bypass jet engines). Planar laser-induced fluorescence will be utilized to obtain planar scalar measurements at three downstream locations: $x/D_{in} = 2, 5$ and 10. To serve as a benchmark, planar measurements will also be obtained at the same downstream locations for a simple jet with $Re = 6700$. Radial profiles of the mean, root-mean-square (rms) and skewness of the concentration, as well as probability density functions, will be presented and discussed for both jet configurations (simple and coaxial).

A secondary objective related to multi-scalar mixing has also been established. In an experiment conducted in the same facility, Lavertu (2008) performed simultaneous measurements of two homogenously pre-mixed scalars in a simple jet. His work focused on quantifying the effects arising from differing molecular diffusivities during the mixing process. These effects are referred to as differential diffusion effects and, though they often occur at very small scales, they can impact certain processes when not accounted for (such as a loss in efficiency during combustion). A long-term objective of this research project is to perform differential diffusion measurements inside a coaxial jet. To this end, locations within the coaxial jet structure where differential diffusion effects could be important will be determined using single scalar measurements.

1.3 Organization of Thesis

The remainder of the thesis will be structured as follows. In Chapter 2, a review of the relevant theoretical considerations and literature will be presented. The topics of discussion will consist of: the properties of turbulent flows, turbulent

jets (simple and coaxial), scalar mixing in turbulent jets and, finally, laser-induced fluorescence.

Chapter 3 will describe the experimental methods. Firstly, the design of the coaxial nozzle will be presented, followed by a description of the flow control apparatus. The optical set-up, including the laser sheet generation system and the light detection system, will then be described. This will be followed by an overview of the data acquisition, post-processing and calibration procedures. The chapter will conclude with an examination of the potential sources of error and the steps taken to minimize them.

Chapter 4 will provide a description of the flow validation procedure, the experimental conditions and the uncertainty analysis. In the first section, simple jet measurements from the present work will be compared to past works to validate the turbulent jet structure and the measurement technique. The experimental conditions will then be presented and justified. The chapter will end with an uncertainty analysis quantifying the uncertainty in the concentration measurements.

In Chapter 5, the results consisting of radial profiles of the mean, rms and skewness of the concentration, as well as probability density functions, will be presented. The radial profiles will be considered first followed by the probability density functions. Throughout the chapter the results will be physically interpreted and discussed.

In the final chapter of this thesis, Chapter 6, the conclusions of the current work will be presented. Firstly, the main findings will be summarized and their relation to the project's objectives and practical applications will be highlighted. Finally, recommendations for future work will be provided and the novel contributions of this work will be presented.

Chapter 2: Theoretical Considerations & Literature Review

As a comprehensive overview of turbulence is beyond the scope of this paper, this chapter will only discuss the most relevant topics. The first section will review some theoretical considerations related to turbulence and the remainder of the chapter will consist of a literature review pertaining to: turbulent jets, multi-scalar mixing in jets and laser-induced fluorescence. The reader is referred to the texts by Tennekes and Lumley (1972) and Pope (2000) for a more detailed description of turbulence.

2.1 Theoretical Considerations

As Tennekes and Lumley (1972) remarked in their seminal textbook: "…it is very difficult to put a precise definition to turbulence." However, turbulent flows do posses many common characteristics, notably: large Reynolds numbers, randomly fluctuating flow variables, high levels of transport (of momentum, heat, mass) and a continuum of scales (both in length and in time). These turbulent flow characteristics are inherently interrelated and will now be described in greater detail.

In 1883, Osborne Reynolds performed an experiment where he injected dye into a flow of clear water contained in a pipe. The transition from laminar to turbulent flow was studied and he concluded that the dimensionless number formed from U_0, D and ν (i.e., the Reynolds number) was the most useful parameter to predict this transition. Since then, many similar experiments have been undertaken resulting in an agreed upon rule of thumb that internal flows possessing

$Re > 2000$ will exhibit turbulent flow characteristics. It is possible for the transition to turbulence to occur at higher Reynolds numbers by limiting sources of flow instabilities in the experimental set-up. Turbulence, however, cannot be sustained at low Reynolds numbers. If considering a scalar quantity transported by a turbulent flow, the level of mixing and molecular smearing increases with the Reynolds number. However, beyond the so-called *mixing transition,* the flow can no longer create additional interfacial area between scalars to aid in mixing and the flow is considered fully turbulent. Dimotakis (2000) concluded in his work that the mixing transition occurs over a relatively narrow range of Reynolds numbers ($10000 < Re < 20000$) for several types of flows (shear layers, jets) and can therefore be considered a universal phenomenon of turbulence.

The Reynolds number is a critical parameter in predicting turbulent behavior because it describes how instabilities are dissipated in a flow. As was mentioned in Chapter 1, the Reynolds number represents the ratio of the inertial forces to the viscous forces. At low Reynolds number, naturally occurring flow instabilities at all scales are quickly dampened out by viscosity. However, these instabilities persist in high Reynolds number flows, where the viscous forces are relatively small compared to the inertial forces. Due to the presence of the instabilities, variables such as velocity, pressure, temperature or mass concentration begin to fluctuate randomly about their mean value. This important turbulent flow characteristic has the overall effect of increasing momentum, heat and mass transport. The random nature of this process makes statistical analysis essential to the study of turbulence.

The flow instabilities described above manifest themselves as vortices, or eddies, spanning a continuum of length and time scales. Energy to sustain their development is provided by the mean flow, where shearing action caused by mean velocity gradients produces large energy containing eddies. Through vortex stretching, these large eddies then break up into progressively smaller and less energetic ones. This process continues until the kinetic energy of the smallest eddies is dissipated by viscosity. The energy transfer from the largest to smallest scales in

turbulent flows is referred to as the *turbulent energy cascade*. The largest scales of the cascade, or integral scales, are governed by the geometry of the flow; and the smallest scales, referred to as the Kolmogorov microscales, are a function of the viscosity of the fluid and the rate at which turbulent kinetic energy is dissipated per unit mass (ε).

Kolmogorov (1941) formalized this concept by proposing two hypotheses. Firstly, he theorized that for flows of sufficiently high Reynolds number, the directionality of the large scale eddies (governed by flow geometry and initial conditions) is lost at smaller scales and the flow becomes locally isotropic. As a result, various turbulent flows (jets, wakes, boundary layers, etc.) should exhibit a universal behavior determined uniquely by ν and ε at scales much smaller than the integral scales. Secondly, he proposed that at sufficiently high Reynolds number, an intermediate region of scales called the *inertial subrange* forms between the integral scales and Kolmogorov scales. In the inertial subrange, viscous action should be negligible, leading to a behavior determined uniquely by ε. These two hypotheses have been experimentally confirmed for many different turbulent flows.

2.2 Turbulent Jets

The turbulent flow studied in this experiment is that of a steady state, momentum-driven, axisymmetric, coaxial jet. It is however useful to review simple jets before discussing coaxial jets, as these two flows share many features.

2.2.1 Simple Jets

An ideal, steady-state, momentum-driven, axisymmetric, simple jet can be described as: a fluid steadily flowing out of a round nozzle of diameter "D" into a quiescent background (Pope 2000). Any density differences between the jet and

background fluids are neglected. Different exit velocity profiles are possible, though the fully developed pipe flow and the top-hat velocity profiles are the most common. Such a flow is categorized as a *free shear* flow; i.e., a flow that arises from mean velocity gradients and is far removed from obstacles such as walls (Pope 2000). Other examples of free shear flows include shear layers and wakes. In these flows, the boundary layer approximations can be used, which assume that the radial gradients are much larger than the axial gradients $\left(\frac{\partial}{\partial x} \ll \frac{\partial}{\partial r}\right)$ (Pope 2000). Therefore, in the case of a statistically stationary, momentum-driven, axisymmetric, turbulent simple jet, the mean continuity and mean momentum equations reduce to:

$$\frac{\partial \langle U \rangle}{\partial x} + \frac{1}{r}\frac{\partial (r\langle V \rangle)}{\partial r} = 0 \tag{2.1}$$

$$\langle U \rangle \frac{\partial \langle U \rangle}{\partial x} + \langle V \rangle \frac{\partial \langle U \rangle}{\partial r} = \frac{\nu}{r}\frac{\partial}{\partial r}\left(r\frac{\partial \langle U \rangle}{\partial r}\right) - \frac{1}{r}\frac{\partial}{\partial r}(r\langle uv \rangle)\,, \tag{2.2}$$

where x represents the axial (or downstream) direction, r represents the radial direction, U is the instantaneous axial velocity, u is the fluctuating axial velocity, V is the instantaneous radial velocity, v is the fluctuating radial velocity and $\langle \cdot \rangle$ denotes averaging in time. We have assumed no mean velocity in the azimuthal direction, θ (i.e., no swirl).

When considering the velocity field in the downstream direction, a simple jet can be divided into 2 regions: the developing and self-similar regions. In the developing region, a shear layer forms between the ambient fluid and the jet fluid (also referred to as the jet core) as the flow exits the nozzle. This shear layer grows radially both inwards and outwards as the jet progresses downstream until it fully consumes the jet core. Once this occurs, the flow will tend to a self-similar state. The

downstream location after which self-similarity is reached depends on which quantity is being considered; the mean velocities reach self-similarity before the fluctuating components of velocity (Wygnanski and Fiedler 1969). It is generally agreed that the mean velocity reaches self-similarity after $x/D = 30$, while the root-mean-square of the velocity reaches self-similarity after $x/D = 70$ (Hussein, Capp and George 1994, Xu and Antonia 2002, Ball *et al.* 2012).

In the self-similar region, the mean centerline velocity $\left(U_{mean,CL}\right)$ is inversely proportional to the downstream distance $\left(U_{mean,CL} \sim x^{-1}\right)$ and the velocity half-width $\left(r_{1/2}\right)$, which represents the radial position where $U = \frac{1}{2}U_{mean,CL}$, is proportional to the downstream distance $\left(r_{1/2} \sim x\right)$ (Pope 2000). As a result, the local Reynolds number $\left(Re_0(x) = \frac{U_{mean,CL} \cdot r_{1/2}}{\nu}\right)$ is independent of x in the self-similar region. Finally, in the self-similar region, the centerline turbulence intensity of the axial velocity, defined as: $(u_{rms}/U_{mean})_{CL}$, has been experimentally shown to converge to a value of approximately 0.24 (Panchapekesan and Lumley 1993a).

The above describes the general behavior of an axisymmetric jet. However, the effect of initial conditions (*Re* and nozzle exit velocity profiles) on the rates of radial growth and centerline velocity decay in the self-similar region remains a source of debate. If the idea of *universal self-similarity* is correct, the self-similar region should only depend on the initial jet momentum and not on its initial conditions. However, growing evidence seems to point towards *local self-similarity,* where many possible self-similar states exist, depending on the initial conditions of the jet (Ball *et al.* 2012).

While the effect of initial conditions on the velocity field have not been fully determined and remains a source of debate in the self-similar region, initial conditions are undoubtedly important in the developing region. For example, Xu and Antonia (2002) showed that a jet with a top-hat exit velocity profile tended to develop and reach self-similarity before a jet with a fully developed pipe flow exit

velocity. Despite the fact that the developing region can be important in many applications, such as in jet engine design, researchers have tended to focus of the self-similar region. Nevertheless, some studies have specifically investigated the velocity field in the developing region.

Ko and Davies (1971) used hot-wire anemometry to make velocity measurements inside the jet core ($x/D < 4$) of a simple jet of air. The fluctuating velocity component (u_{rms}) was measured within the jet core at various radial and axial locations. The authors observed an increase in u_{rms} both as the measurements extended radially from the jet centerline towards the jet core boundary and as measurements were made at increasing downstream distances. The authors also varied the Reynolds number and found that u_{rms} generally increased with increasing Re, while still following the above-mentioned trends.

Fellouah *et al.* (2009) used stationary and flying hot wire anemometry to make velocity measurements in the developing region of a turbulent jet of air at varying Reynolds numbers ($6000 < Re < 30000$). In all Re cases, the mean centerline velocity remained constant until $x/D \approx 6$ (i.e., end of the jet core), after which it decayed with the downstream distance $\left(U_{mean,CL} \sim x^{-1}\right)$. The fluctuating velocity components (u_{rms}, v_{rms}) had a bimodal radial distribution in the developing region, with the location of each peak corresponding to that of the center of the shear layer surrounding the jet core. Reynolds number effects were most notable when considering the velocity spectra. In the developing region at both the centerline and at $r/D = 1/2$, the inertial subrange became more prominent with increasing Re.

In many practical applications, jets are a transport medium for scalars. Much like the velocity field, the scalar field of turbulent jets also has a tendency towards self-similarity after an initial development region. This was investigated by Wilson and Danckwerts (1964) who used resistance thermometry to measure the

temperature field of a heated jet of air ($Pr \sim 1$) emitted into a quiescent background. They found that the mean temperature excess (ΔT_{mean}, defined as the temperature difference between the jet air and the background air), became self-similar for $x/D > 10$, and the fluctuating temperature excess (Δt_{rms}), beyond $x/D = 40$. The axial mean temperature excess followed a x^{-1} decay law and the jet half-width increased as x^1. The fluctuating temperature excess normalized by the mean temperature excess along the centerline $\left(\Delta t_{rms}/\Delta T_{mean,}\right)_{CL}$, which is also referred to as the centerline temperature turbulence intensity, converged to a value of 0.18 in the self-similar region for all Reynolds numbers ($10000 \leq Re \leq 40000$). They went on to highlight the role played by the Schmidt (or Prandtl) number when comparing liquid and gaseous flows. They concluded that under the same flow conditions, the cut-off point, defined as the axial distance from the nozzle where the concentration has been diluted to a certain value, was 9% farther downstream in a liquid jet than in a gas jet.

Becker *et al.* (1967) used a light scattering technique to measure the concentration field of oil smoke ($Sc = 38000$) in a jet of air emitted into a quiescent background. They found that the mean concentration (C_{mean}) became self-similar for $x/D > 20$, and the fluctuating concentration (c_{rms}), beyond $x/D = 40$. In this region, the axial mean concentration obeyed an x^{-1} decay law, the jet half-width increased as x^1 and the centerline concentration turbulence intensity $\left(c_{rms}/C_{mean,}\right)_{CL}$ had converged to a value of 0.22. One-dimensional scalar power spectra were measured along the jet centerline and exhibited the expected $-5/3$ power law slope in the self-similar region.

Dowling and Dimotakis (1990) used a Rayleigh scattering technique to measure the concentration field inside a gas jet ($Sc \sim 1$) emitted into a slow gaseous co-flow (to prevent reverse flow) for $5000 < Re < 40000$. The centerline turbulence intensity converged to a value of approximately 0.23 in the self-similar region, independent of the Reynolds number. Interestingly, increases in Re or Sc

lead to a broadening of the c_{rms} radial profile. They justified this finding by identifying the product "$Re \cdot Sc$" as an inverse measure of "diffusive smoothing or smearing" of the concentration field. They explained that as Sc increases, molecular diffusion effects become less strong, leading to less smoothing or smearing of the scalar field (note that these effects still happen, but at a much smaller scale). As Re increases, parcels of high concentration dye at the edge of the jet are re-entrained into the jet more quickly. This reduces the time available for diffusion to occur. In summary, they concluded that as the product "$Re \cdot Sc$" increases one would expect more significant fluctuations near the edge of the jet due to reduced molecular diffusive smearing of the field. Dowling and Dimotakis went on to measure the scalar spectrum over the range of Re stated above. Along the centerline, the spectra exhibited the $-5/3$ power law slope in the self-similar region. The range of the power law region shifted to higher frequencies as the Re increased. The probability density functions were plotted in the self-similar region at various radial positions. The centerline PDFs (at $x/D = 20, 40, 60, 80$) showed that no ambient fluid had reached the centerline. This was not the case in the high Schmidt number experiment ($Sc \approx 700$) performed by Dahm (1985), where they observed ambient fluid along the centerline.

Miller and Dimotakis (1991) used point laser-induced fluorescence to measure the concentration field of sodium fluorescein ($Sc \sim 1000$) within a turbulent liquid jet emitted into a quiescent background for $3000 < Re < 24000$. Most notably, they observed that the centerline turbulence intensity scaled inversely with Re, asymptotically approaching the value of 0.23 at high Re (past the mixing transition point). This behavior differed from that of Dowling and Dimotakis (1990), where the centerline turbulence intensity converged to 0.23 for all Re due to the nominally unity value of Sc in their experiment.

Mi *et al.* (2001) studied the effect of exit velocity profile on the downstream evolution of a heated jet of air emitted into a quiescent background. Two different nozzle geometries were tested: a converging nozzle, producing and top-hat exit

velocity profile and a constant area nozzle, producing a fully developed pipe flow exit velocity profile. Cold-wire thermometry was used to perform instantaneous temperature measurements and hot wire thermometry was used to make velocity measurements. Both the developing and self-similar regions were investigated.

Based on their flow visualizations (oil droplets illuminated by a laser sheet), there existed fundamental differences in the flow structure within the developing region for each exit velocity profile. For the jet issuing from the converging nozzle, large-scale coherent structures were present immediately downstream and acted to entrain large amounts of ambient fluid towards the centerline, whereas these structures were not present for the jet issuing from a constant area nozzle. As a result, mixing between the jet and ambient fluid was increased for the jet issuing from a converging nozzle when compared to the jet issuing from a constant area nozzle, effectively shortening the developing region. The entrainment of ambient fluid by these large-scale structures resulted in a peak in turbulence intensity along the jet centerline immediately downstream of the end of the inner core for the jet issuing from the converging nozzle. The centerline probability density functions revealed that more ambient fluid was present in the jet issuing from a converging nozzle than in the jet issuing from the constant area nozzle.

In the self-similar region, the value of the centerline turbulence intensity eventually reached an asymptotic value for both jets, but its magnitude was smaller for the jet issuing from the constant area nozzle. Higher entrainment of ambient fluid led to higher radial spreading rates and higher centerline mean concentration decay rates for the jet issuing from a converging nozzle. The jet Reynolds number was also observed to have an impact on the decay rate of the jet issuing from the converging nozzle, but not the jet issuing from the constant area nozzle. The authors theorized that the structures formed in the developing region as a result of the initial conditions are propagated downstream and affect the self-similar state.

2.2.2 Coaxial Jets

In the discussion on simple jets, the effect of various geometric and flow conditions was considered. While these trends remain true for coaxial jets, the situation is substantially complicated by the appearance of two additional variables: the velocity ratio (r_v) and the area ratio $\left(A_{o/i}\right)$. The velocity ratio is defined as the ratio between the average exit velocity of the outer and inner jets $\left(r_v \equiv \frac{U_{0,out}}{U_{0,in}}\right)$ and, likewise, the area ratio is defined as the ratio between the areas of the outer and inner nozzle $\left(A_{o/i} \equiv \frac{A_{out}}{A_{in}}\right)$.

Figure 2. 1 is a schematic of the developing region of a typical coaxial jet with the main features labeled. Immediately after the flow exits the nozzle, two cores form and eventually disappear as the jet progresses downstream and the inner and outer shear layers grow. This process usually occurs in the region $x/D_{in} < 10$. Farther downstream, the coaxial jet will then tend to a self-similar state equivalent to that reached by a simple jet of same total momentum (Champagne and Wygnanski 1971). It is worth briefly noting that this last statement may not universally hold if the flow exhibits local self-similarity, such that initial conditions play a role is the final self-similar state of a jet (Hussein, Capp and George 1994, Xu and Antonia 2002, Mi *et al.* 2001, Ball *et al.* 2012). Nevertheless these issues are of secondary concern for the current work as only the developing region was investigated.

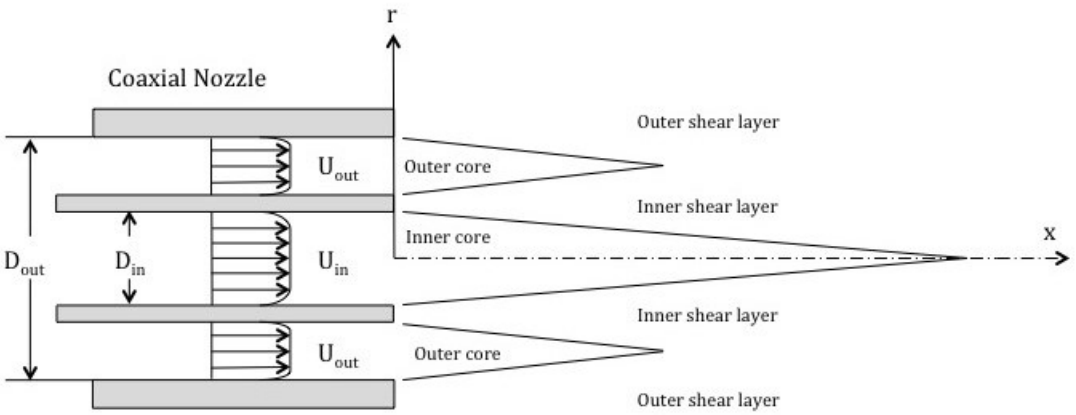

Figure 2. 1: Schematic representation of the developing region of a coaxial jet.

The developing region of coaxial jets has been extensively studied since the dawn of the space age due to its importance in the design of coaxial fuel injectors. In these studies, often the velocity field has been the main focus and a wealth of resources documenting its behavior exists; the main papers are summarized below. Surprisingly, comparatively little work has been done investigating the scalar field, however the relevant papers are also presented.

Champagne and Wygnanski (1971) were the first to systematically attempt to characterize the velocity field of coaxial jets. They used 2 constant temperature hot-wire anemometers to make velocity measurements spanning both the developing and self-similar region of a coaxial jet of air with: $0 < r_v < 10$ and $A_{o/i} = 1.28$ and 2.94. As the flow developed in the downstream direction, they observed that the mean and fluctuating velocities became self-preserving after $x/D_{out} \approx 40$ for all r_v and $A_{o/i}$ (where D_{out} denotes the outer diameter of the nozzle). In this region, the centerline velocity decay and radial growth rates were insensitive to both the velocity and the area ratios. In the developing region however, the inner core length was dependent on both the velocity and the area ratios. Champagne and Wygnanski noted that a larger area ratio resulted in a longer inner core, though the

effect was small compared to varying the velocity ratio. As the velocity ratio was decreased from 10 to 1, the core length was substantially increased. This was most likely due to reduced shear between the two (inner and outer) flows. For $r_v < 1$, the core remained roughly the same length as for $r_v = 1$. A peak in centerline turbulence intensity of the axial and radial velocities $(u_{rms}/U_{mean}\,, v_{rms}/V_{mean})_{CL}$ was observed immediately downstream of the termination of the core, similar to the observations of Mi *et al.* (2001), who measured a peak in $(t_{rms}/T_{mean})_{CL}$ immediately downstream of the termination of the jet core for a simple jet. Mi *et al.* (2001) concluded that this feature was unique to jets produced by converging nozzles, which was also the type of jet used in Champagne and Wygnanski's experiment.

Ribeiro and Whitelaw (1976) used hot wire anemometry to measure the developing region ($x/D_{out} < 30$) of a coaxial jet of air with: $r_v = 1$ and $A_{o/i} = 5.8$. Similar to Champagne and Wygnanski (1971), both the axial and radial centerline turbulence intensities exhibited a maximum after the termination of the inner core, with the peak in the radial fluctuation being more pronounced. The radial profiles of fluctuating velocity were characterized by 2 peaks, one for each shear layer.

Ko and Kwan (1976) used constant temperature hot wire anemometry to study the developing region ($x/D_{out} < 4.5$) of a coaxial jet of air with $r_v = 0.3, 0.5$ and 0.7 and $A_{o/i} = 2.67$. In their work, they divided the developing region into 3 distinct sub-regions, each corresponding to a different core/ shear layer arrangement: i) the initial merging zone, which contains both cores and both shear layers; ii) the intermediate zone, which contains only the inner core (as the inner and outer shear layers have merged); iii) the fully-merged zone, in which the inner core disappears and the coaxial jet tends towards simple jet behavior. The transition from one zone to another occurs at downstream locations that are principally a function of the velocity ratio and, to a lesser extent, the area ratio. It was found that at downstream distances lying within the initial mixing zone and the fully-merged zone, the mean velocity profile was self-similar inside both the inner and outer

shear layers (when appropriately normalized). However, no self-similarity was observed in the intermediate mixing zone. These results agreed with prior measurements performed inside the shear layer of simple jets (Ko and Davis, 1971). The authors also described the flow structures within the shear layers by way of radial pressure and velocity spectra at several locations within the jet. The velocity spectra revealed 2 types of vortices, each possessing different characteristic frequencies. The radial pressure distributions revealed that the high frequency (or primary) vortices were located inside the inner shear layer and that the low frequency (or secondary) vortices were located inside the outer shear layer. Depending on the velocity ratio, the relative strength of the vortices varied. For $r_v = 0.3$, the fast inner jet produced strong primary vortices, which tended to dominate the downstream flow. However, for $r_v = 0.7$ the secondary vortices dominated the downstream flow.

Ko and Au (1981) extended the above work by making velocity measurements in the developing region of a coaxial jet of air with velocity ratios larger than 1. The area ratio was: $A_{o/i} = 2.73$ and the velocity ratios were: $r_v = 1.25, 1.67$ and 2.50. The length of the outer core remained relatively constant for all r_v values and was equal to approximately $1.7D_{out}$. However, the length of the inner core was a function of the velocity ratio and varied from $2.1D_{out}$ to $4.1D_{out}$. Similar to the results of Champagne and Wygnanski (1971), the inner core length increased as the velocity ratio tended to 1. For downstream distances spanning all three regions described in their previous work (Ko and Kwan 1976), the mean velocity profile exhibited self-similarity inside the outer shear layer. The inner shear layer, however, only exhibited self-similarity in the initial merging zone.

Dahm *et al.* (1992) used 2-color planar laser-induced fluorescence to image the developing region of a coaxial jet of water. Rhodamine B and disodium fluorescein were used as fluorescent dyes and the jet was visualized in the axial direction. The jet had a fixed area ratio of 0.94 and the velocity ratio was varied

from 0.59 to 4.16. The authors were investigating the qualitative properties of turbulent structures in the outer and inner shear layers, whose presence was alluded to by the works of Ko and Kwan (1975) and Ko and Au (1981). They described the velocity profile of a coaxial jet as a superposition of a wake-like profile and a shear-like profile, each contributing their own kind of instabilities. Wake-like instabilities can have circulation in both senses, whereas shear-like instabilities possess structures with the same circulation sign. They observed that when $r_v = 0.59$ and 0.71, the outer shear layer formed shear-like instabilities which were able to deform the inner shear layer, though the inner instabilities never had a chance to fully develop before the end of inner core. As a result, the downstream flow was dominated by the outer shear layer structures. For $r_v = 1$ and 1.14, the inner shear layer formed a wake-like profile, with wake-like instabilities initially forming, but quickly pairing with the outer shear layer structures. For $r_v = 2.56$ and 4.16, both shear layers formed shear-like instabilities, which had opposite circulation and became locked near the nozzle exit. The effect of absolute velocity was also investigated by comparing two jets, each with $r_v = 1$, but with differing absolute velocities. In both cases, the outer layer exhibited the expected shear-like instabilities. Interestingly, increasing the velocity resulted in better developed wake-like instabilities in the inner layer, which would eventually interact with the outer layer.

Rehab *et al.* (1997) used hot wire anemometry and planar laser-induced fluorescence to make velocity and scalar measurements in the developing region of a coaxial jet of water at high velocity ratio ($1 < r_v < \infty$) and an area ratio of 1.82. This marked the first study investigating the scalar field of a coaxial jet at high Schmidt number ($Sc \sim 2000$). A primary goal of the work was to investigate the effect of high velocity ratios on the inner core characteristics, up to the limit of a purely annular jet ($r_v = \infty$). At low velocity ratios ($1 < r_v < 7$), the inner core length was inversely proportional to r_v, while the outer core length remained constant for all r_v. The flow visualization revealed the expected shear-like instabilities in both shear layers, which quickly locked and acted to entrain ambient fluid into the core.

When $r_v \approx 7$ however, a recirculation regime formed, marked by the formation of a recirculation cavity. In this region, backflow from the outer jet fluid was observed in the inner jet. The authors related the formation of the cavity to a balance between the turbulent shear stress gradient driving the flow forward and the adverse axial pressure gradient decelerating the flow. They described that the length of the recirculation cavity increased as r_v tended to infinity ($U_{in} \to 0$), up to a maximum length of $x/D_{in} = 1$.

Villermaux and Rehab (2000) continued investigating coaxial jets given their application in airblast atomization, a process characterized by a high momentum outer jet surrounding a slower inner jet. Using the same set-up and measurement system as their previous study (see Rehab *et al.* (1997)), the scalar field at high velocity ratios was studied in detail. They defined the mean concentration thickness as: $\delta_C = \frac{C_0}{\left({}^{dC_{mean}}/_{dr}\right)_{max}}$, where C_0 represents the initial concentration and $\left({}^{dC_{mean}}/_{dr}\right)_{max}$ represents the largest gradient in mean concentration across the entire shear layer. This measure gives an indication of the width of the shear layer. They found that the concentration thickness increased exponentially in the axial direction until reaching a stable plateau at a downstream location corresponding to the first roll-up. The dilution length, L_d (the axial distance corresponding to a predetermined centerline concentration decay) was found to be inversely proportional to the velocity ratio for several centerline concentration decays. They also measured the probability density function at a radial location corresponding to the middle of inner shear layer for many downstream locations. Close to the nozzle exit, the PDF was bimodal with peaks corresponding to the initial inner jet concentration ($C = C_0$) and the outer jet concentration ($C = 0$). The two peaks quickly merged into one as the flow progressed downstream. Interestingly, the unimodal PDFs all possessed positive skewness, indicating a higher probability of high concentration fluid. This was related to the presence of high concentration lamellae, pealed off from the inner jet and entrained into the shear layer.

In perhaps the most thorough and complete treatment of coaxial jets to date, Schumaker and Driscoll (2011) studied the scalar field of coaxial gaseous jets in a plethora of configurations. Planar laser-induced fluorescence (PLIF) with the inner jet seeded with an acetone marker was used as a measurement technique. Parameters such as the density ratio $\left(S = \frac{\rho_{out}}{\rho_{in}}\right)$, the velocity ratio, the area ratio and the Reynolds number were systematically varied. As the density ratio decreased (i.e., increasing the inner jet's momentum), the inner core length increased and the decay of the mean axial mixing fraction was reduced. The area ratio did not affect the development region within the limited range tested $\left(A_{o/i} = 3.0 \text{ and } 5.3\right)$. For all jet configurations, the centerline fluctuating mixing fraction was initially zero for downstream distances less than 5 inner jet diameters, but quickly increased as outer fluid was entrained to the centerline. After a peak, which was relatively similar in magnitude for all density and velocity ratios, the fluctuating values began to decay as the two streams became increasingly well mixed. The radial fluctuating profiles exhibited the expected double peak in the developing region, due to the presence of an inner and outer shear layer in the flow. Interestingly, when comparing high ($\sim$ 19000) and low ($\sim$ 3400) Reynolds numbers, it was observed that mixing was in general reduced at high Re (longer inner core length). This was attributed to necking in the outer jet flow, which occurred within the first few inner diameters, followed by a rapid shear layer growth for the low Re jets. In summary, this work confirmed most of the already established trends relating to velocity ratio, density ratio and area ratio. Nevertheless, the large number of experiments performed for a range of different configurations makes this work a very useful database for scalar measurements in the developing region of coaxial jets.

2.2.3 Multi-Scalar Mixing in Turbulent Jets

Until now, only single scalar mixing in turbulent jets has been considered. As was mentioned to in the introduction, however, multi-scalar mixing is a more representative process for certain applications, but has received significantly less attention. In this section, two research projects, one performing multi-scalar mixing in a simple jet and another in a coaxial jet, will be summarized.

Lavertu *et al.* (2008) used laser-induced fluorescence to measure differential diffusion effects in a simple jet of water. In their experiment, two scalars (denoted by C_1 and C_2) of differing molecular diffusivities were initially pre-mixed in the flow and measurements were made in the self-similar region. This work primarily investigated the Reynolds number dependence and the radial distribution of differential diffusion effects, while the largest scale at which these effects persisted was also of particular interest. A parameter called the normalized concentration difference $\left(Z \equiv \frac{C_1}{C_{1,mean}} - \frac{C_2}{C_{2,mean}}\right)$ was used to quantify instantaneous differences in scalar concentration between both scalars. The time series of Z along the jet centerline for $Re = 900$ and 10600 revealed that differential diffusion effects persisted for periods of time longer than the Kolmogorov time scale and that their magnitude increased as Re decreased. Lavertu *et al.* (2008) proceeded to quantify the magnitude of the differential diffusion effects by measuring the root-mean square of the normalized concentration difference (z_{rms}). They determined that the value of z_{rms} decreased with increasing Reynolds, while the radial distribution of z_{rms} increased in the radial direction (for all Reynolds numbers). These two trends were related to ambient fluid entrainment at the measurement location. The probability density functions of Z measured at the jet centerline were effectively Gaussian, whereas those measured off-axis had positive skewness. The positive skewness was said to be the result of the more diffusive scalar diffusing more rapidly out of a parcel of dyed fluid into a parcel of ambient fluid than the less diffusive one.

Multi-scalar measurements in pre-mixed flows allow some multi-scalar effects (such as differential diffusion) to be more easily isolated and studied. Nevertheless, to better approximate the true mixing in a coaxial injector, Cai *et al.* (2011) studied the scalar field of a coaxial jet with one scalar in the inner flow and a different scalar in the outer flow. Planar laser-induced fluorescence was used to make measurements on the inner jet, which consisted of air seeded with acetone, and planar laser Rayleigh scattering was used to make measurements on the outer ethylene jet. The velocity ratio was 0.94, the area ratio was 1.30 and the density ratio was 1.07. For both scalars, the centerline turbulence intensity eventually asymptoted to the value of 0.21 as the jet approached self-similarity. The correlation coefficient between the scalars was calculated to infer the level of mixing between the two scalars and the ambient air. The correlation coefficient was calculated along the jet centerline and radially at various downstream locations in the developing region. Along the jet centerline and where the ambient air had yet to penetrate, the correlation coefficient was equal to -1. As the jet progressed downstream, the centerline correlation coefficient began to increase as air was slowly mixed. When the scalars were fully mixed at the molecular level, the centerline correlation coefficient was equal to +1 since both scalars were perfectly correlated and mixing together with the air. In the radial direction, the correlation coefficient varied from -1 at the jet centerline to +1 near the edge of the jet for all downstream locations in the developing region.

For a more complete overview of the literature specifically concerned with multi-scalar mixing in coaxial jets, the reader is referred to the works of: Cabra *et al.* (2005), Rowinski and Pope (2013) and Li *et al.* (2017).

2.3 Laser-Induced Fluorescence

The discussion will now shift from turbulent jets to the measurement technique used in this work, laser-induced fluorescence (LIF). Laser-induced fluorescence is a technique that measures the light emitted by a fluorescent material when it is excited by a laser. Fluorescence occurs when electrons are excited to a higher energy state and then return to a lower energy state, emitting a photon in the process. The wavelength of the emitted photons is always longer than the wavelength of the excitation source, a phenomenon referred to as the Stokes shift. This shift allows experimentalists to detect and quantify the light emitted by fluorescent molecules dissolved in a fluid, enabling instantaneous species concentration measurements. The non-intrusive nature of the technique and the high spatial and temporal resolution offered by LIF make it a powerful tool for studying turbulent flows.

The concentration (C) of a species is related to the emitted fluorescence intensity (I) by way of the following formula (Guilbault, 1973):

$$I = \Phi_f I_0 (1 - e^{-\beta b C}), \tag{2.3}$$

where Φ_f is the quantum efficiency, I_0 is the incident radiant power, β is the molar absorptivity and b is the path length of the cell. If using dilute dye concentrations ($\beta b C \ll 1$), a first order Taylor expansion can be performed and equation 2.3 simplifies to:

$$I = \Phi_f I_0 \beta b C. \tag{2.4}$$

This form reveals that with constant laser power (and dilute dye concentrations), the species concentration becomes linearly related to the emitted fluorescence intensity. For simplicity, experiments are typically conducted in this range.

The works of Owen (1976) and Dewey (1976) initiated the widespread use of LIF as a measurement technique in fluid mechanics. Since then, a variety of experiments have been performed, each with their own unique approach. Early examples include: Breidenthal (1981), Dyer and Crosley (1982), Kychakoff *et al.* (1982), Koochesfahani (1984), and Walker (1987). More recent studies include: Villermaux and Rehab (2000), Lavertu *et al.* (2008), Cai, *et al.* (2011), Schumaker and Driscoll (2012), and Perez-Alvarado (2016), among others. The LIF-related details of each experiment are unique, and thus a brief overview of the existing methods will be provided.

The most common excitation source is a continuous wave argon-ion laser, though pulsed Nd:YAG lasers have recently been utilized (Cai, *et al.* 2011, Schumaker and Driscoll 2012, Vanderweel and Tavoularis 2014). Fluorescence measurements can be obtained: i) at a point by focusing the beam (Saylor and Sreenivasan 1998, Lavertu *et al.* 2008), ii) along a line on a section of the beam (Dahm and Dimotakis 1990), iii) on a plane by either expanding the beam through a cylindrical lens (Dahm and Dimotakis 1987, Guillard *et al.* 1998, Cai, *et al.* 2011) or by scanning the beam using a rotating mirror (Gaskin 1996, Villermaux and Rehab 2000, Perez-Alvarado, 2016); or finally iv) inside a volume by sweeping a laser sheet (Buch and Dahm, 1996, Vliet *et al.*, 2004) .

LIF measurements can be performed in air, but this technique is most commonly used in water. The most common fluorescent tracer used in air is acetone (Cai *et al.* 2011, Schumaker and Driscoll 2012). In water, tracers include: disodium fluorescein (Dahm and Dimotakis 1990, Saylor and Sreenivasan 1998, Lavertu *et al.* 2008, Perez-Alvarado *et al.* 2016), fluorescein dextran (Saylor and Sreenivasan 1998), basic blue (Saylor and Sreenivasan 1998), sulforhodamine 101 (Lavertu *et al.*

2008) and rhodamine 6G (Gaskin and Wood 2001). The emitted fluorescence can be detected by using: a photodiode (Koochesfahani 1984, Dowling *et al.* 1989), a photomultiplier tube (or PTM) (Saylor and Sreenivasan 1998, Lavertu *et al.* 2008) or a CCD camera (Gaskin 1996, Villermaux *et al.* 2000, Cai *et al.* 2011, Perez-Alvarado 2016).

Over the years, several research groups have improved the measurement techniques used in LIF. Walker (1986) thoroughly investigated the emitted fluorescence of disodium fluorescein as a function of laser power, solvent pH, and solvent temperature. The dye was dissolved in water and was then irradiated by an argon-ion laser. Within the range of 0 to 0.3 W, the emitted fluorescence increased linearly with laser power. Temperature effects were small: on the order of a 1% reduction in emitted fluorescence per $1°C$ change in temperature. Interestingly, the effect of water pH was extremely significant, especially in the range of $pH = 6$ to 8. In fact, Walker concluded that a buffer solution of $pH > 8.5$ should be used when performing LIF measurements to mitigate this sensitivity. Laser attenuation, which refers to the loss in laser power as the fluorescent dye absorbs energy, was also investigated. Walker concluded that attenuation effects were negligible if dilute dye concentrations were used ($\sim 10^{-7}M$). Lavertu (2008) also performed laser attenuation tests and came to the same conclusion.

Another common source of error encountered in LIF is photobleaching. This occurs when the emitted fluorescence of a substance decreases after constant laser irradiation. Saylor (1995) investigated photobleaching of disodium fluorescein dissolved in water. A dilute concentration of dye ($10^{-6}M$) was dissolved in still water and was irradiated by an argon-ion laser with an output power of 1W. He measured a reduction in fluorescence intensity of more than 50% after approximately 10 ms of constant laser irradiation. This effect was still significant, though reduced when the laser was pulsed, indicating some level of reversibility in the photobleaching process. Using a very similar measurement set-up, though higher laser power, Lavertu (2008) observed a 50% reduction in emitted

fluorescence for disodium fluorescein after approximately 20 ms of constant irradiation.

Wang and Fielder (2000a) investigated photobleaching as well as thermal blooming of disodium fluorescein solutions. Thermal blooming refers to the decrease in emitted fluorescence as the dye becomes hotter (usually due to laser irradiation). Typically the effects of photobleaching and thermal blooming are difficult to isolate, and their combined effect is, therefore, measured. Dilute dye concentrations ($\sim 10^{-6} M$) in water were irradiated by a 5 W argon-ion laser and the laser power, fluid velocity and dye concentration were systematically varied. Lower laser powers, faster flow rates and lower dye concentrations all contributed to a reduction in the cumulative effect of photobleaching and thermal blooming.

In another experiment, Wang and Fielder (2000b) investigated the signal to noise ratio (SNR) of the fluorescent light emitted by a 4 μm^3 control volume. Naturally, the small volume emitted very little light, which resulted in a low SNR. To increase the signal, the laser power and dye concentration were increased, though this led to an increase in photobleaching and thermal blooming. They concluded that an understanding of these competing effects was, therefore, important when establishing the LIF parameters in an experiment.

Lavertu (2008) investigated photomultiplier drift, which refers to a decrease in the output voltage of these devices with time. He noticed this phenomenon occurring with his PMTs most noticeably during the first few minutes after being turned on. The voltage would then stabilize over a period of approximately 10 minutes. As a result, the PMTs were warmed in the presence of a light source before performing measurements.

Chapter 3: Experimental Methods

The present chapter will discuss the methods used throughout this project. The first sections will describe the experimental facility, the hydraulic set-up and the measurement system. The data acquisition, data post-processing, and calibration procedures will then be described. Finally the main sources of error will be considered.

3.1 Experimental Facility

Experiments were conducted in a 6 m by 1.5 m by 1 m glass tank located in the Environmental Hydraulics Laboratory of the Department of Civil Engineering and Applied Mechanics at McGill University. The sides of the tank consisted of single 1.91 cm thick tempered glass panes, the bottom consisted of two stacked panes and the top was left open. The tank was filled with filtered and softened water from the building's main water supply. Its temperature was regularly checked and ensured to be within $\pm$ 2 $°C$ of the ambient temperature. The tank was filled slowly to reduce currents and once full, the water was allotted 3 hours to become quiescent prior to an experiment. The entire experimental set-up was contained inside a darkroom designed to minimize light interference. To this end, all the walls were painted black, black curtains covered the windows and experiments were conducted with the lights turned off (Figure 3.1).

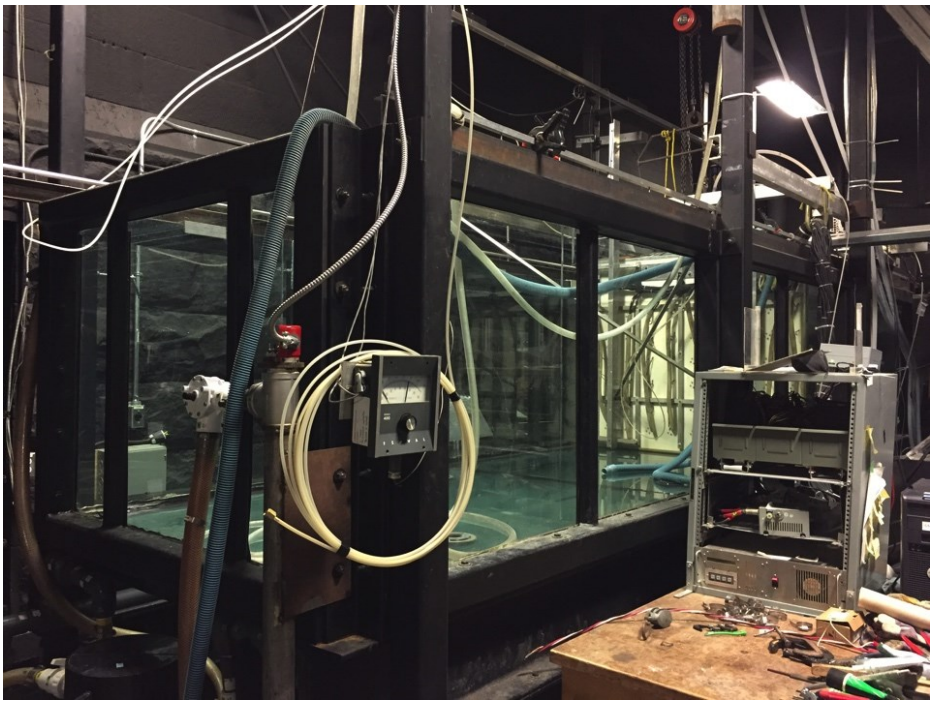

Figure 3.1: Glass tank inside the darkroom.

3.2 Hydraulic Set-Up

A hydraulic set-up, consisting of a coaxial nozzle and a flow control apparatus, was constructed to produce an axisymmetric and steady coaxial jet with a controllable volumetric flow rate and velocity ratio. In this section, the coaxial nozzle will first be described, followed by an overview of the flow control apparatus.

3.2.1 Coaxial Nozzle

The coaxial nozzle in this work consisted of two concentric straight tubes, thus forming a *fixed area* nozzle (as opposed to a *converging area* nozzle). The inner tube had an inner diameter (ID) of 8.51 *mm* and an outer diameter (OD) of 9.52 *mm*, while the outer tube had an ID of 16.6 *mm* and an OD of 19.1 *mm*. These dimensions resulted in a nozzle with an inner hydraulic diameter of 8.51 *mm*, an outer hydraulic

diameter of 7.08 mm, an area ratio of 2.55 and a diameter ratio of 1.95. The tubes were made of smooth bore seamless stainless steel tubing and were cut in house to the appropriate length.

To ensure an axisymmetric jet, it was necessary to: firstly, have fully developed pipe flow at the nozzle exit, and secondly, minimize vibrations and deflections along the nozzle. With this in mind, a lower bound for the tube length was determined by calculating the entrance length, which represents the minimum distance required to achieve fully developed internal flow. The following empirical relation was used to estimate the entrance length (L_e) as a function of hydraulic diameter (D_H) and Reynolds number (Re):

$$\frac{L_e}{D_H} \approx 4.4Re^{1/6} . \tag{3.1}$$

Since the entrance length increases with Reynolds number, a conservative value of $Re = 7000$ was used to calculate the inner and outer entrance lengths (recall that during an experiment, $Re_{in} = 6700$ and $Re_{out} = 5500$). As depicted in Figure 3.2, the manner with which the coaxial nozzle was assembled resulted in a much longer inner tube than outer tube. This meant that fully developed pipe flow was inevitably achieved in the inner tube, making the outer tube the limiting factor. The outer tube was therefore cut to 150 mm, which was slightly longer than its entrance length ($L_{e,out} = 136\ mm$), thus ensuring fully develop pipe flow, while also minimizing deflections and vibrations.

To assemble the coaxial nozzle, the outer and inner tubes were concentrically fastened through a combination of compression fittings and a tee fitting, as depicted in Figure 3.2. One compression fitting secured the outer tube to the tee and two others were used in series to secure the inner tube and to minimize deflections.

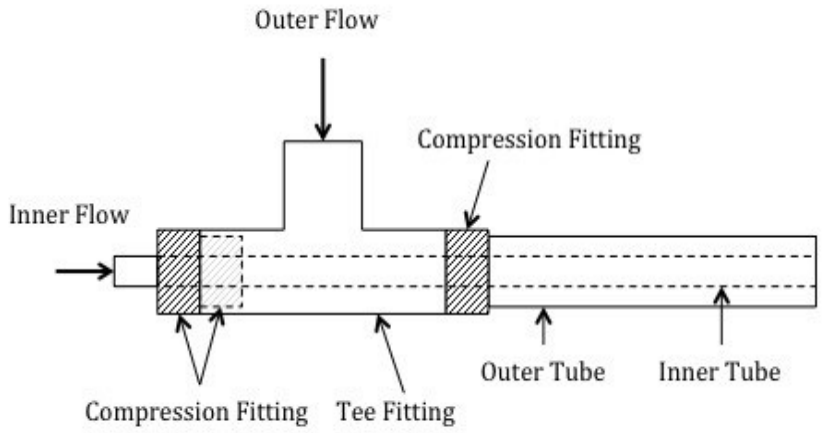

Figure 3.2: Sketch of the coaxial nozzle *(not to scale)*.

3.2.2 Flow Control Apparatus

The flow control apparatus accomplished the following 3 goals: it produced steady flow through both the inner and outer tubes of the coaxial nozzle, allowed for flow rate control through each tube independently and enabled linear displacement of the whole nozzle in each of the Cartesian directions (x, y and z). Figure 3.3 is a schematic of the flow control apparatus for one of the jets. In practice, two nearly identical apparatuses worked in parallel to produce independent flow through the coaxial nozzle. Each component will now be described and any small differences between the inner and outer apparatuses will be highlighted.

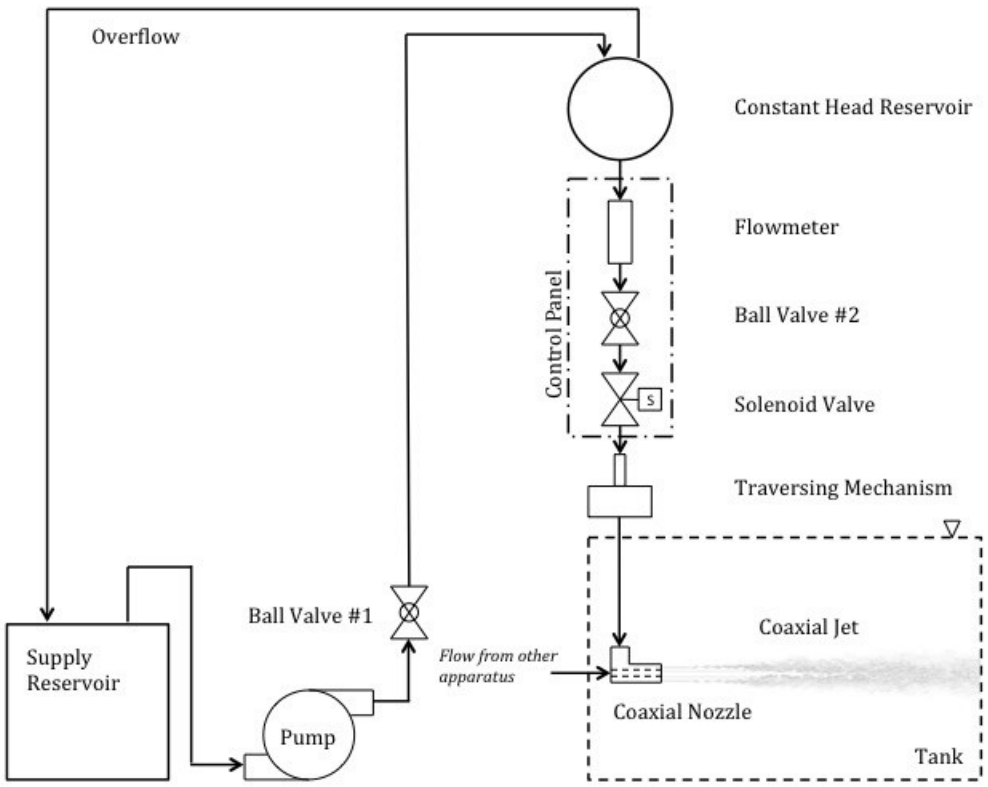

Figure 3.3: Schematic of the hydraulic set-up, only one apparatus is depicted for clarity (*not to scale*).

Water was supplied to the coaxial nozzle from 2 identical 54 L glass supply reservoirs, one for the inner jet apparatus and one for the outer jet apparatus. They were placed on the floor providing easy access for mixing with fluorescent dye prior to experiments. Water was continually pumped from the supply reservoirs to the constant head reservoirs through 19.1 mm ID food-grade PVC tubing. The flowrate was controlled via a ball valve placed at the pump outlet. A 1/3 HP centrifugal pump (Franklin Electic) was used for the inner jet apparatus and a 1/3 HP centrifugal pump (Little Giant) was used for the outer jet apparatus. Figure 3.4 is photograph of the pumps connected to the supply reservoirs.

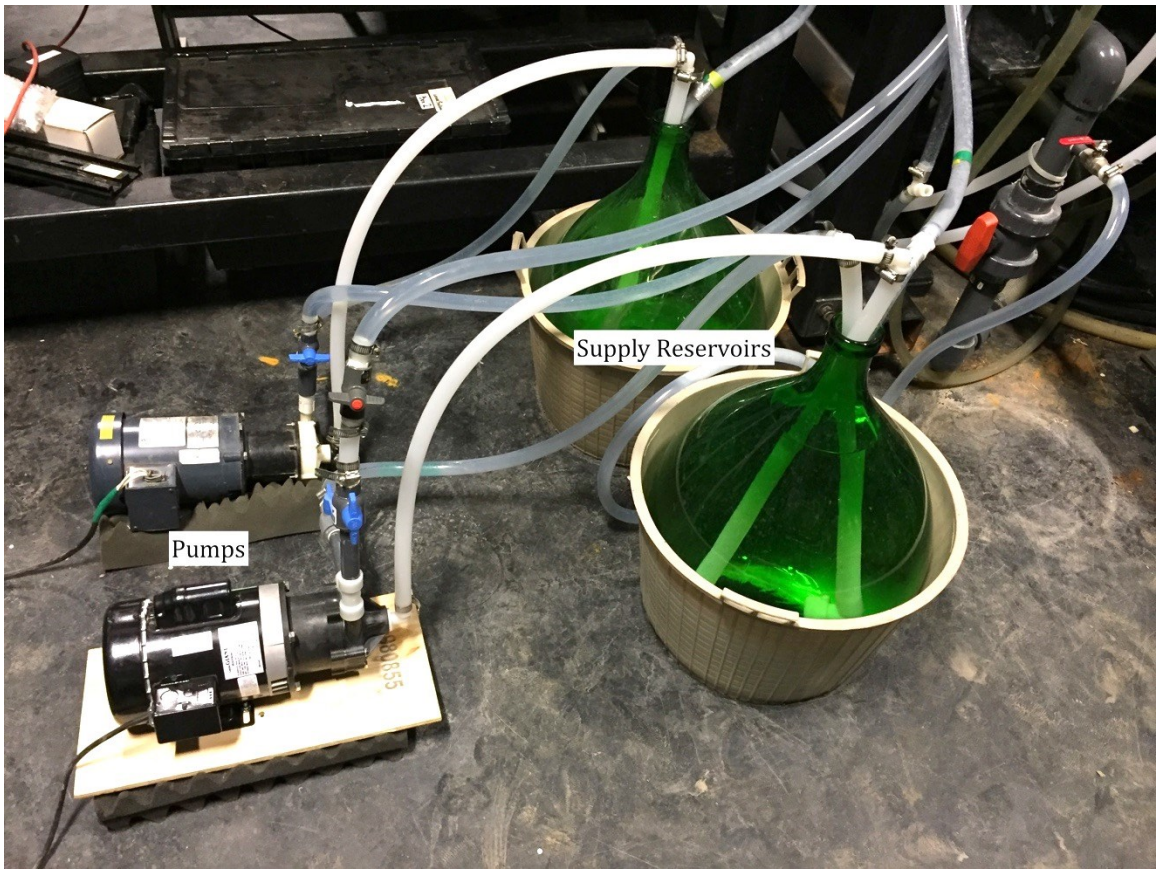

Figure 3.4: Pumps connected to the supply reservoirs.

The constant head reservoirs consisted of two identical 12 L spherical glass containers located 3 m above the nozzle exit and allowed for a steady flow rate of water through the coaxial nozzle. To connect the required tubing to the constant head reservoirs, each one was modified to include an opening at the top and two outlets (one near the top and the other at the bottom). The opening at the top served as a water inlet from the pump, the top outlet served as the overflow, and the bottom outlet eventually led to the nozzle (see Figure 3.5). To ensure a steady flow of water through the coaxial nozzle, the water level in the reservoirs was kept constant by pumping water through the inlet at a flow rate that was slightly higher than the flow rate exiting through the bottom outlet.

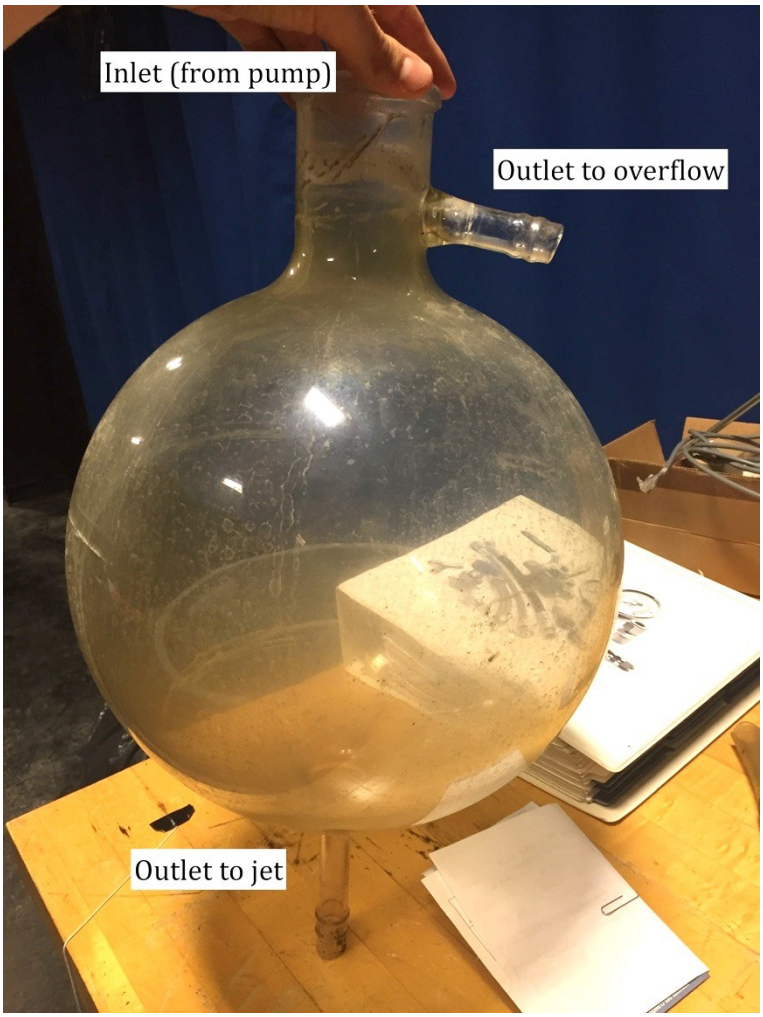

Figure 3.5: Constant head reservoir.

Two control panels were designed and built for the purpose of controlling the volumetric flow rate through the coaxial nozzle and to turn the flow on and off. Each panel consisted of a flowmeter, a ball valve and a solenoid valve, connected in series using rigid 19.1 mm PVC pipes (see Figure 3.6). The ball valve and flowmeter (McMaster Carr, 8051K44) were used in tandem to set the volumetric flow rate (and therefore Reynolds number). The accuracy of the flowmeters was $\pm$ 2% full scale. The solenoid valve (McMaster Carr, 4629K14) was used to control whether or not there was flow through the nozzle. When no voltage was applied, the valve was closed and the flow rate was 0 (i.e., normally closed). Conversely, when a voltage was applied (by closing a switch), the valve opened and allowed flow to pass.

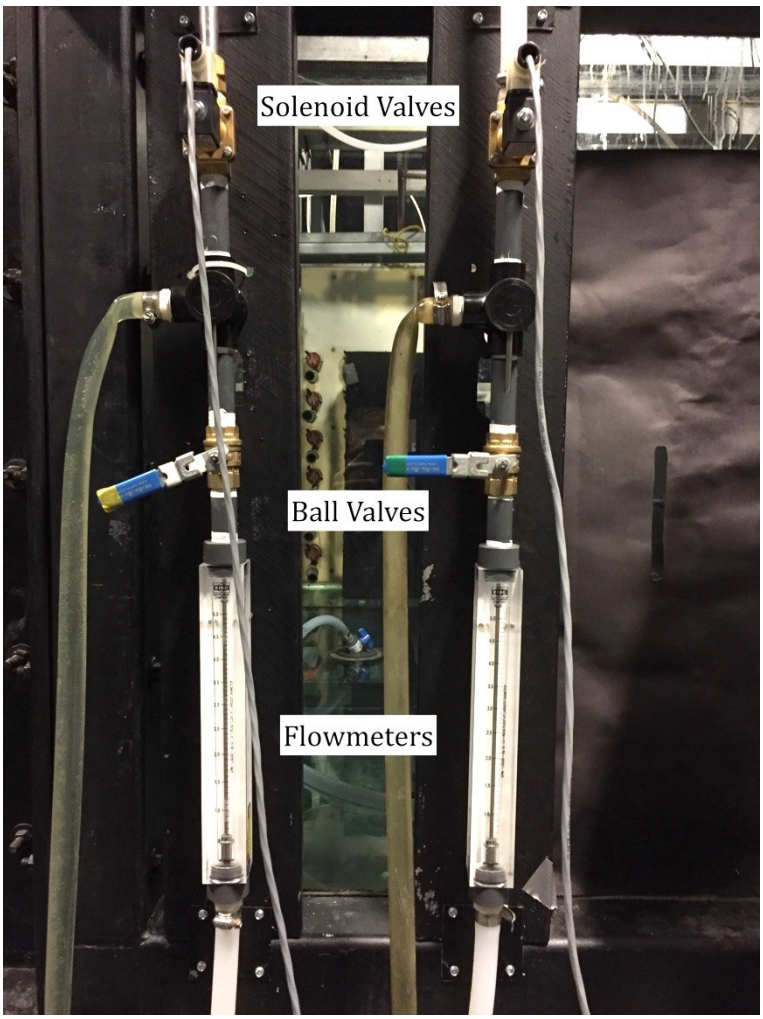

Figure 3.6: Control panels.

The flow leaving each control panel was then fed to the inner or outer tubes of the coaxial nozzle. A different sequence of tubing for both the inner and outer flows was necessary to accommodate the different tube diameters that formed the coaxial nozzle (see Figure 3.2). The inner flow exited the solenoid valve through 16.6 *mm* ID stainless steel tubing, which was then connected to 7.94 *mm* food-grade polyethylene tubing. The tubing was then directly connected to the inner jet tube through an elbow fitting. The outer flow exited the solenoid valve through 19.1 *mm* polyethylene tubing. This tubing then connected to the top of a vertical 2 *m*, 16.6 *mm* ID stainless steel tube. This tube extended down into the tank and

connected to the top of the tee. As a result, this tube and the coaxial nozzle formed a rigid connection that could be moved as a unit.

Linear translations of the nozzle were necessary during the alignment of the optics and during experiments to make different axial and radial measurements. This was accomplished using a Velmex traversing mechanism. The traversing mechanism was capable of producing independent movement in each Cartesian direction (x, y and z), with a specific assembly associated to each direction. Each assembly was driven by a motor and consisted of a base, a carriage, and a lead screw. The assemblies were orthogonally aligned and fastened to a C-channel carriage capable of rolling on tracks in the y-direction. Figure 3.7 summarizes these main features. The motors were controlled using a VXM-2 stepper motor controller and a custom LabVIEW program and the movement resolution was 0.05 mm in all directions. The displacement range was 130 cm in the x-direction, 24 cm in the y-direction and 55 cm in the z-direction. Limit switches and mechanical stoppers were placed at the base of each assembly to avoid collisions.

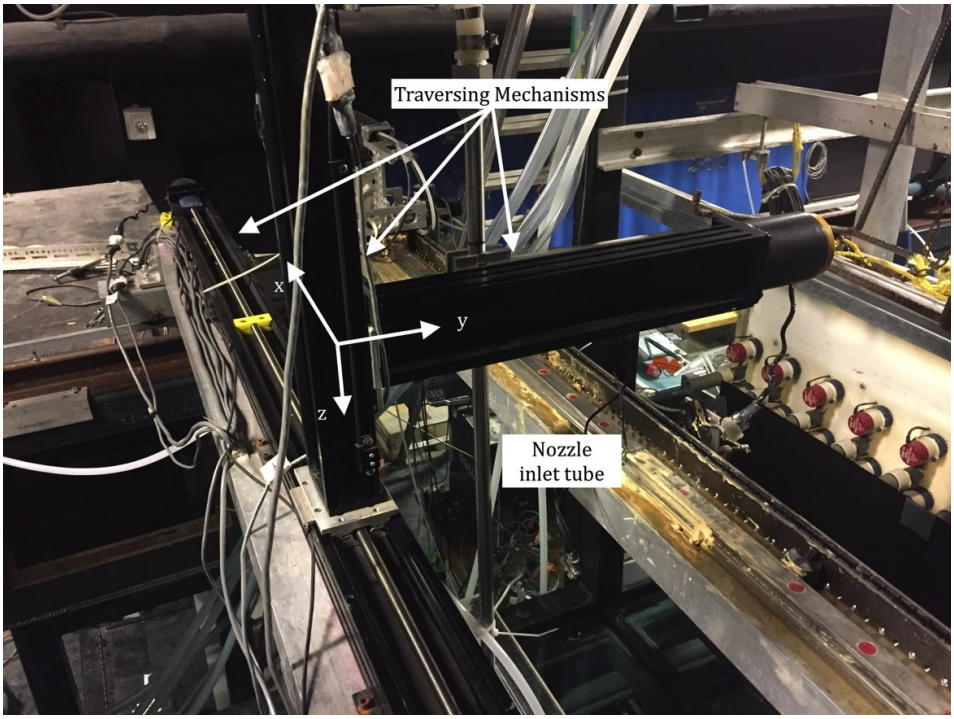

Figure 3.7: Traversing mechanism.

3.3 Optical Set-Up

An optical set-up, consisting of a laser sheet generation system and a light detection system, was assembled to produce and capture the fluorescent signal. The laser sheet generation system consisted of a laser, two mirrors, and a laser scanning device. The light detection system consisted of a camera, an image intensifier, a camera lens, and an optical filter. Figure 3.8 outlines the main components.

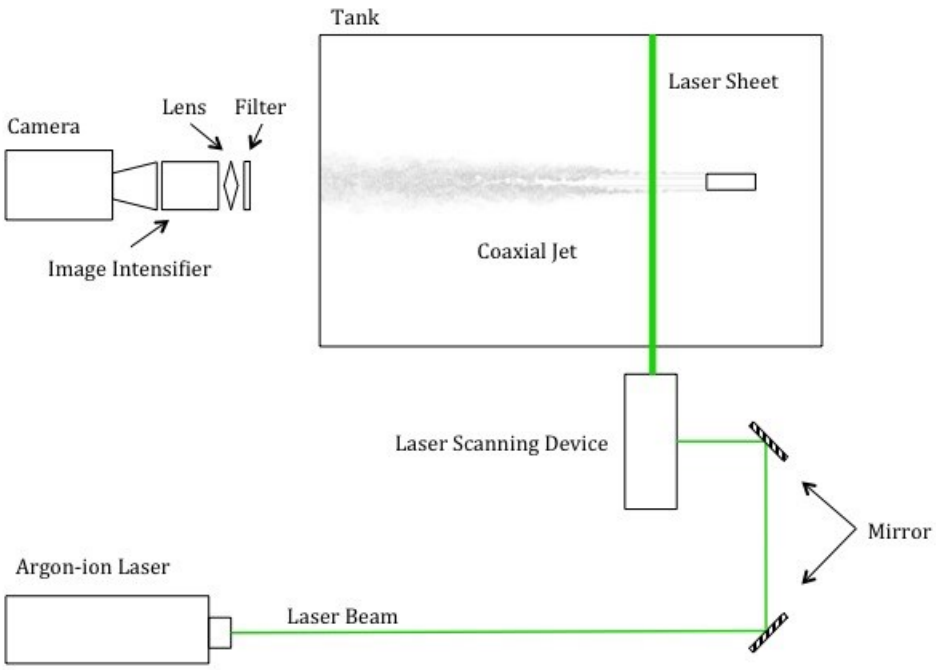

Figure 3.8: Schematic of the planar LIF system, top-view (*not to scale*).

Radial cross-sections of the coaxial jet were irradiated by laser light, which was rapidly scanned in the laser sheet generating system to form of a 2-dimensional laser sheet. An argon-ion laser (Coherent Innova 90) was used to produce the beam, which was Gaussian in cross-section. The aperture was set to 3.97 *mm* and the

wavelength to 514.5 nm. The laser was warmed up for 60 minutes before each use and was operated in light regulation mode to provide power stability ($\pm$ 0.5%). The power was measured before and after each experiment using a power meter (Coherent Lasermate), which was accurate to $\pm$5 % and a typical experiment was conducted using a beam with an output of 0.6 W.

A laser scanning device was used to scan the beam and produce a 2-dimensional laser sheet. The beam was directed from the laser into the device using two mirrors (Melles Griot, 02MLQ003/009). The scanning device consisted of a 12.7 mm diameter dielectric mirror (Newport, 5151), a 1.5 m focal length plano-convex lens (PLCX-25.4-772.6-C) and a rotating mirror (Lincoln Laser Company, DT-08-236-019), all fastened to an aluminum casing (see Figure 3.9). Upon entering the laser scanning device, the beam was reflected off the dielectric mirror, through the laser focusing lens, into the rotating mirror assembly.

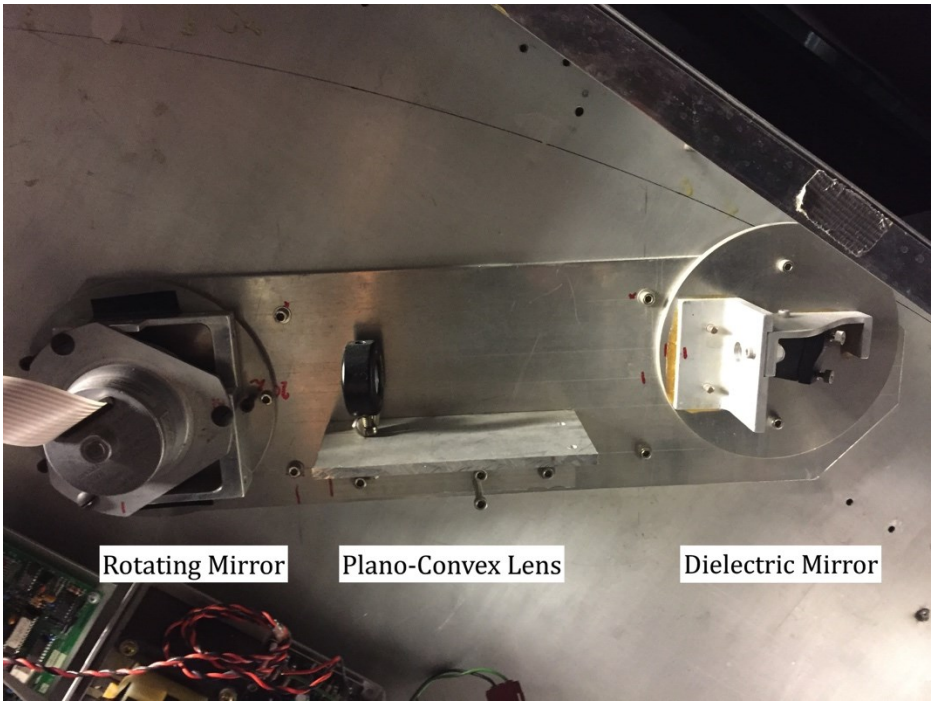

Figure 3.9: Laser scanning device.

The laser focusing lens focused the beam down to a waist diameter (d_0) of 470 μm and had a Rayleigh range (Z_R), defined as the distance at which the focused beam increases to $\sqrt{2}$ the waist diameter, of 22.7 cm. These value were determined as follows (Ready 1978):

$$d_0 = \frac{2.44 f \lambda}{D_b} \tag{3.2}$$

$$Z_R = \frac{\pi f^2 \lambda}{D_b}, \tag{3.3}$$

where f is the lens focal length, λ is the wavelength of light, and D_b is the laser beam diameter. The jet was placed such that the focal point corresponded to jet centerline.

The rotating mirror assembly consisted of an 8-sided polygonal mirror (Lincoln Laser Company, DT-08-236-019) mounted to a motor rotating at 12000 rpm. This effectively created a 2-dimensional sheet by scanning the incident laser beam 1600 times every second. This method of generating a laser sheet was selected for 2 reasons: scanning the beam created a sheet of uniform intensity and the rapid scanning minimized thermal blooming and photobleaching effects (see §3.6). A cylindrical lens, a common alternative, would have produced a sheet of Gaussian intensity profile and would have required a chopper to control the exposure time of the dye to laser light.

The following steps were followed to align the components making up the laser sheet generating system. The angles of incidence on the two mirrors in Figure 3.8 were such that the beam entered the laser scanning device incident on the dielectric mirror. Coarse placement of the mirrors was accomplished by moving the magnetic bases to which they were mounted and fine adjustments were accomplished using the adjustment screws. The components inside the laser

scanning device were already mounted in-line with each other, therefore, only fine adjustments (using adjustment screws) of the dielectric mirror were required to bring the beam incident on the rotating mirror. The device was then turned on and the sheet was generated. Using the traversing mechanism, the tip of the coaxial nozzle was placed on the same plane as the laser sheet, such that only the front of the nozzle was illuminated. The nozzle was then moved 100 mm in the vertical (z) direction and any drift of the nozzle's tip out of the laser sheet's plane was noted. Shims were then placed under the base of the laser scanning device to correct any misalignment in the z-direction. The nozzle was then moved 100 mm in the horizontal (y) direction and the entire laser-scanning device was pivoted to correct any misalignments. At times, the vertical and horizontal adjustments resulted in the laser beam no longer coming into contact with the dielectric mirror; the process was therefore iterative in nature. The laser and one mirror were placed on the same table, while the second mirror and the laser scanning device were placed on a different table. The feet of both these tables rested on 25.4 mm thick Sorbothane dampers, which reduced the effect of vibrations on the optical set-up.

The fluorescence emitted by the dye as it crossed the laser sheet was captured by the light detection system, which consisted of: an optical filter, a camera lens, an image intensifier and a high-speed camera (Figure 3.10).

Figure 3.10: Light detection system.

During experiments, it was important to capture light from the emitted fluorescence only and not scattered laser light. As such, the light signal (fluorescence and scattered laser light) passed through a $2'' \times 2''$, $550\ nm$ colored, long-pass, glass filter (ThorLabs, FGL550S) placed in front of the other components. Any light of wavelength greater than $550\ nm$ was transmitted through this filter, while light of lower wavelength was blocked. The laser operated at $514.5\ nm$ and the fluorescent dye (disodium fluorescein) emitted light between $480\ nm$ and $650\ nm$ in wavelength. As a result, any scattered laser light was blocked and wavelengths associated to dye's fluorescence were transmitted through the filter (at approximately 90% transmission for $\lambda \geq 600$). In practice some scattered laser light was transmitted through the filter, as an ideal filter is not a physical possibility. This source of optical noise was, however, deemed negligible in the current work. The filtered light then passed through a camera lens (PENTAX, 50mm f/1.4). This lens was selected because its field of view and focal length allowed for the whole image to be captured in focus. The aperture was set to the maximum value to allow the

greatest amount of light in, thus maximizing the system's sensitivity. After passing through the filter and lens, the light entered the intensifier.

Since the fluorescence signal was very weak, a light intensifier (Video Scope, VS4-1845) was necessary to increase the signal to a level that made full use of the dynamic range of the camera (12-bit). In the light intensifier, the low intensity light first comes into contact with a photocathode. The photocathode then emits electrons, whose energy is greatly amplified by being placed in an electric field (produced by plates held at a high DC voltage difference). The energetic electrons then collide with a micro-channel plate, which induces a cascade of electrons of far greater number than initially emitted by the photocathode. These electrons then collide with a phosphor screen, which emits amplified light. The intensifier's usable range was between 450 and 900 nm, which served the current purpose well. The device was controlled using the VSI image intensifier controller software installed on a DELL XPS computer. The software required 3 inputs: the gate, the gate delay, and the gain. The gate could be set to either "continuous" mode or "pulsed" mode. Continuous mode allowed a continuous flow of electrons through the device. This was the gate state the intensifier was operated in during experiments. Whenever the intensifier was on, but not actively amplifying fluorescent light, it was set to "pulsed" mode to protect it from sudden surges of light. The gate delay was set to 0. The gain was set to values between 65000 and 75000 foot-lambert/foot-candle to optimize the device's performance (i.e., highest signal to noise ratio), as per the manufacturer's recommendation.

The photodetector used in this work was a 12-bit, monochrome camera (pco.dimax). It outputted an image of 2016×2016 pixels in size, with each pixel possessing a grayscale value between 0 and 4095 (i.e., 2^{12}). When coupled with the intensifier, however, the image size was reduced to a circle with a radius of 800 pixels. The intensifier-camera coupling also resulted in uneven light sensitivity across the field of view. As a result, the central region appeared brighter than the

edges, though this effect was accounted for through proper pixel-by-pixel calibration, as will be discussed in §3.5.

To align the light detection system, the following steps were followed. The lights were turned off and a very dim flashlight was directed towards the coaxial nozzle. The camera and intensifier were then turned on and the image of the nozzle was viewed. A dim flashlight was necessary as the intensifier was very sensitive and even ambient light levels could cause irreparable damage. The traversing mechanism was then used in the y and z directions to place the nozzle at the center of the field of view. Recall that the tip of the nozzle was already on the plane of the laser sheet from the alignment of the laser sheet generation system. The focus of the camera lens was then adjusted until the tip of the nozzle was in focus. This ensured that the focal point was located on the laser sheet. The jet was then moved 100 mm in the x-direction and its displacement was recorded by taking a video with the camera. Any drift from the center of the field of view was noted. The camera was then pivoted and/or translated accordingly and the focus was re-adjusted. These steps were repeated until the tip of the nozzle was in focus at the location of the laser sheet and no drift from the center of the field of view was noticed. The whole light detection system was placed on optical rails and tripods, which allowed for easy adjustments. The tripods were placed on a table with 25.4 mm thick Sorbothane dampers under the feet.

The fluorescent dye used in the experiments was disodium fluorescein (Fisher Scientific), which has a Schmidt number of 2000. Figure 3.11 (a) plots the dye's excitation spectra and Figure 3.11 (b) plots the dye's emission spectra (the dashed lines are the spectra for sulforhodamine 101, which was not used in this work). The disodium fluorescein spectra are from measurements of Saylor and Sreenivasan (1998). They, however, used an excitation source of 488 nm, while the current work used a source of 514.5 nm. This would shift the emission spectra towards higher wavelengths, though proper calibration accounted for this effect (see §3.5). To minimize exposure of the dye to light, which could cause it to degrade,

all lights sources in the lab were closed (ceiling lights, desk lamps, cell phones, etc.) and a dim flashlight with a red sheet placed in front of it was used when handling the dye. A batch solution was prepared by dissolving 1 gram of the fluorescent salt in 1 liter of water. Small amounts of this solution were then pipetted into the supply reservoirs and were fully mixed with the water by running the pumps in a recirculating loop. The batch solution was stored in a box, which was placed inside a cabinet. The dye concentration inside the supply reservoirs during a typical experiment was of $7.42 \times 10^{-8}\, mol/L$. Such a diffuse concentration was used for several reasons. Firstly, it ensured that the fluorescent signal was in the linear range. Secondly, it minimized density differences between the dyed and un-dyed fluid. Lastly, it minimized the possibility of trapping and attenuation (see §3.6).

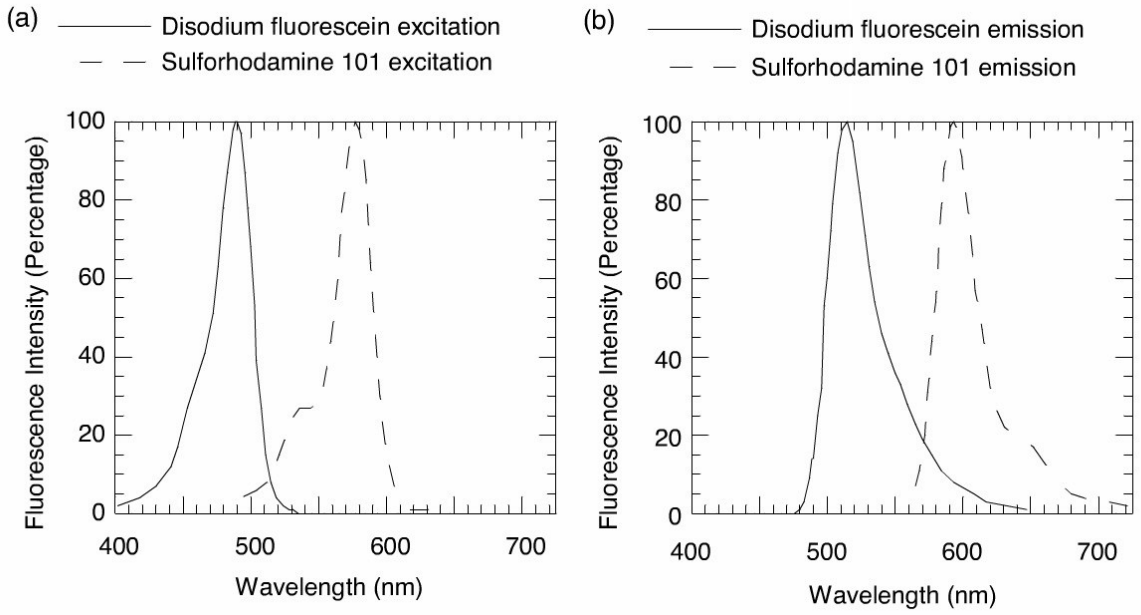

Figure 3.11: Disodium fluorescein fluorescence spectra from Saylor and Sreenivasan (1998). (a) Excitation spectra (solid line). (b) Emission spectra (solid line).

3.4 Data Acquisition and Post-Processing

As was mentioned in §3.3, a high-speed monochrome camera was used to acquire the data in digital form for post-processing. In this subsection, the data acquisition parameters will first be described, followed by a description of the data post-processing procedure.

The fluorescence signal was digitally recorded using a 12-bit monochromatic camera, which was controlled using a software package (Camware). The sampling rate of the camera was set to 30 Hz, the exposure was set to 30 ms and the delay of the exposure was set to 0 s. An exposure time of 30 ms resulted in 48 laser beam scans being recorded per image. This minimized the possibility of observing large variations in the intensity from image to image due to incomplete beam scans over the measurement period. Videos were recorded for 70s, yielding 2104 images per test (when sampled at 30 Hz). The recording time was short enough to ensure dye re-entrainment did not occur and yet long enough to ensure convergence of the mean, rms and skewness of the concentration. The images were initially stored in the internal memory of the camera, then subsequently transferred to the data acquisition computer and finally transferred to an external computer for post-processing.

The images were analyzed using custom codes programmed in MATLAB. The camera outputted files in ".tiff" format, thus the first step was to read these files and convert each image into a 2016×2016 array. Each array was then cropped to eliminate unused space in the field of view and to save memory, resulting in 401×401 arrays. The calibration curves were then applied to each element of the array, converting the grayscale values to mass concentrations (see §3.5 for a detailed description of the pixel-by-pixel calibration procedure).

Each data set was averaged in time to output a 401×401 array containing mean concentration values at each pixel. In a similar manner, higher order moments, such as the standard deviation (or variance) and the skewness, were calculated. These arrays were used to plot the radial profiles of the 3 computed statistical moments of the jet at various downstream locations. Probability density functions at various radial and downstream locations were also computed.

Steps were taken to account for two known sources of error, the presence of repeatable artifacts in the images (such as the outline of the nozzle or the glare of the computer screen) and noise caused by the measurement system's electronics. To this end, before every test, a video of the coaxial nozzle operating at experimental conditions, but with no dye in the flow, was recorded (600 images, sampled at 30 Hz). At every pixel, these images were averaged in time and their variance was calculated yielding a background mean image and a background variance image. The background mean image was subtracted from every image recorded during experiments (with dye in the flow), effectively eliminating stationary and repeatable artifacts that were inadvertently captured by the camera. Using the images obtained during experiments, the variance at each pixel was calculated, producing an un-corrected variance image. The background variance image was subsequently subtracted from the un-corrected variance image, which accounted for electronic noise in the measurement system. After implementing this noise correction method and using gains mentioned in §3.3, the signal to noise ratio ($SNR = \frac{\sigma^2_{signal}}{\sigma^2_{noise}}$) was calculated and ranged from approximately 650 to 20000, depending on which downstream distance and jet configuration were being considered.

3.5 Calibration

A calibration procedure was necessary to relate fluorescence intensity to the dye concentration and to determine the dimensions (in μm) of each pixel. The light detection system described in §3.2 was most sensitive to light in the central part of the image. As a result, a homogenously illuminated sheet captured by the camera would produce an image with a bright center and dimmer edges. To illustrate this, Figure 3.12 (a) is a photograph of a homogenously lit sheet taken during the calibration process ($M = 7.23 \times 10^{-8}\ mol/L$) . The colorbar represents the grayscale. Significant variations in the grayscale are observed across the image and for this reason a pixel by pixel calibration was necessary to determine the calibration curve at each pixel.

(a)

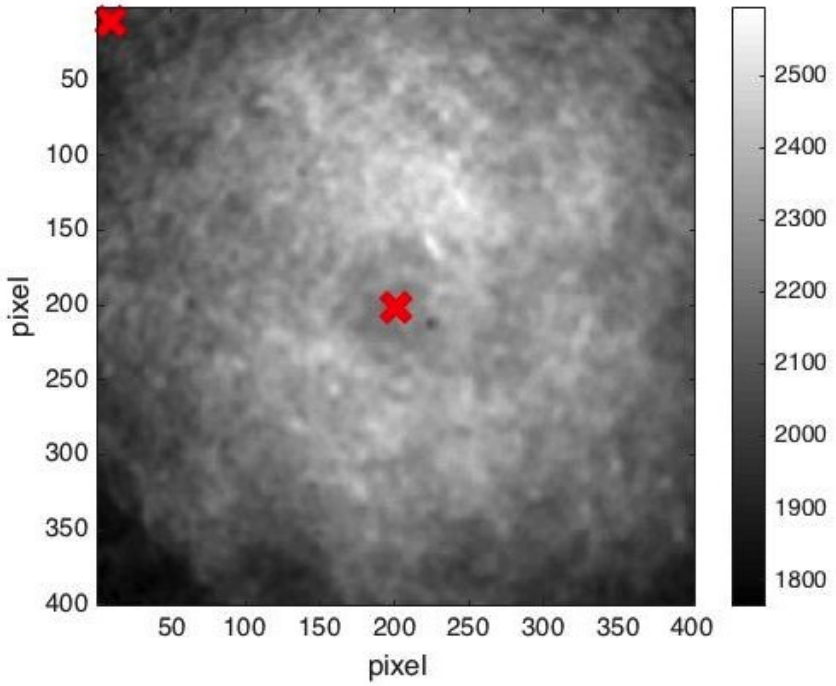

(b)

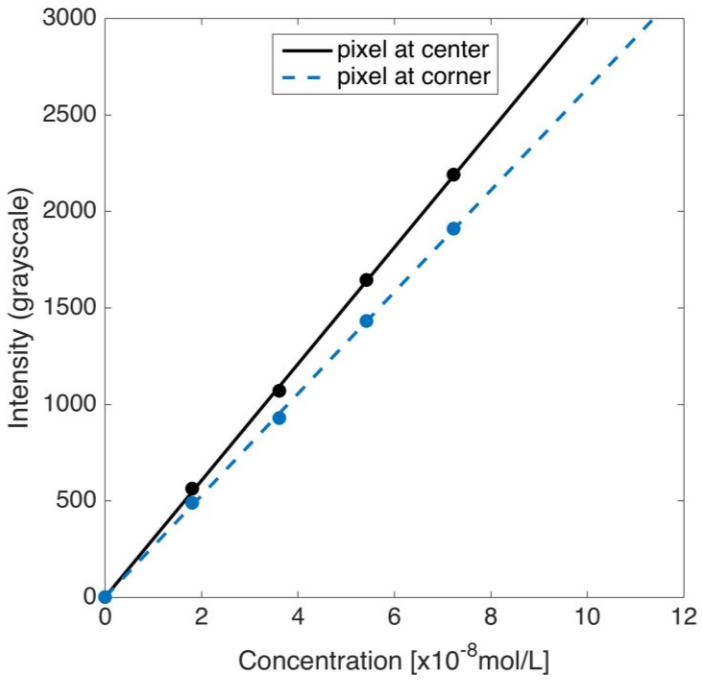

Figure 3.12: (a) Calibration image taken at a dye concentration of $M = 7.23 \times 10^{-8}$ mol/L. Markers (✖) at the pixel location where calibration curves were presented for comparison. (b) Linear calibration curves at two different pixels (– pixel at center, –– pixel at corner).

A calibration box was used, inside which images of the volume of water illuminated by the laser sheet were recorded at progressively increasing and known dye concentrations. Using a box as opposed to the entire glass tank had two advantages. Firstly, the smaller volume resulted in less dye being used. Secondly, trapping and attenuation were minimized since the laser travelled through un-dyed water before reaching the calibration box. The box was 97 L in volume (75 cm $\times$ 30.5 cm $\times$ 42.8 cm) and was made with 6.35 cm thick panes of tempered glass on the sides and a 2.54 cm thick pane on the bottom (the top was open). The calibration box was placed inside the glass tank on top of 4 PVC supports, which raised it to the same level as the light capturing system. The box was placed at a location where it intersected with the laser sheet and the coaxial nozzle was then lowered into it using the traversing mechanism. Both the calibration box and the glass tank were filled with water to the same level. To thoroughly mix the dye, water was cycled from the box through the jet. To this end, the inlet of the pump was connected to the bottom of the calibration box, while the overflow was fastened to the top. Only the inner nozzle was connected to the pump for simplicity. Figure 3.13 is a photograph illustrating the above-mentioned set-up.

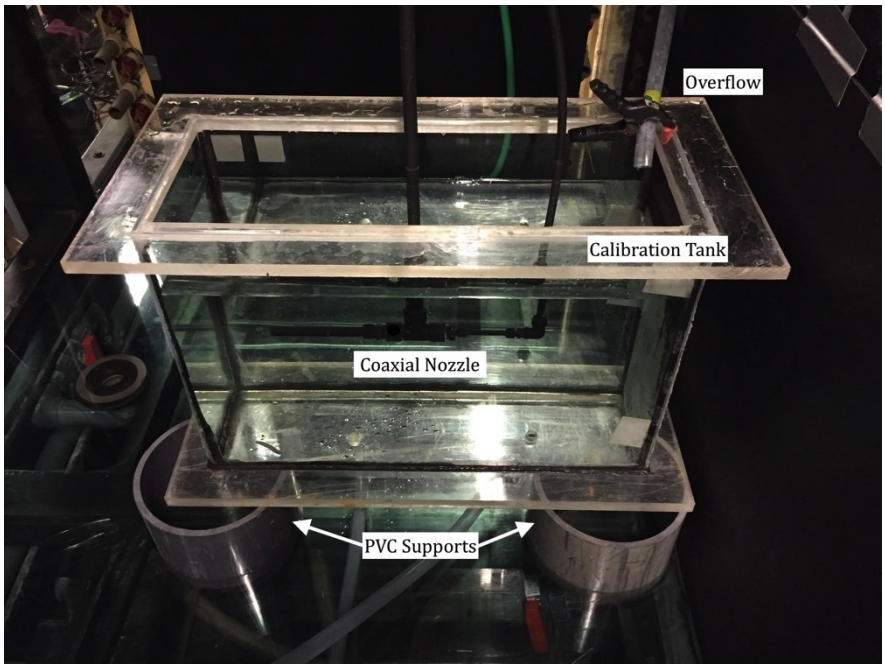

Figure 3.13: Calibration box.

With the calibration box in place and water cycling through the jet, disodium fluorescein was introduced at progressively higher and known concentrations. To ensure homogeneous mixing, the dyed water was cycled through the nozzle for a minimum of 25 minutes at each concentration. Based on the flow rate exiting the inner nozzle, this corresponded to approximately the time required for a full water turnover. The laser sheet was generated and a $45s$ recording was taken for each dye concentration. The optical system's parameters were identical to those used during a typical experiment (see §3.3 and §3.4). Cycling the water through the nozzle produced a significant number of bubbles inside the box, which would then create bright spots in the laser sheet, resulting in erroneously high readings ($\approx 4\%$ increase). The water was therefore allowed 10 minutes to settle before images were recorded.

The images of the progressively higher fluorescence intensities were saved and a pixel by pixel analysis was subsequently performed. A total of five sets of 1315 images were captured, with each set corresponding to a different dye concentration: 0, 1.81, 3.62, 5.43 and 7.24 ($\times 10^{-8}\ M$). The images were processed using a custom code programmed in MATLAB. After cropping and averaging the images in each set, the code fit a line through the concentration vs. intensity (grayscale) data of the following form (for each pixel):

$$C(I) = \mathcal{A}I + \mathcal{B}, \tag{3.4}$$

where C represents the dye concentration, I represents the intensity and $\mathcal{A}$ & $\mathcal{B}$ represent curve fit constants. The constants were stored in arrays and used to convert the camera's output to dye concentration. To illustrate the variation in calibration curves between pixels, Figure 3.12 (b) is a plot of 2 curves, one at the center and another at the corner of the image.

In addition to converting light intensity to dye concentration, it was also necessary to determine the dimension of each pixel (in μm) to obtain physically meaningful radial distances and an estimate of the spatial resolution of the system. To accomplish this, the calibration box was removed and the nozzle was placed such that the tip intersected the laser sheet. A ruler, which was oriented horizontally and located in the same plane as the laser sheet, was then fastened to the tip and a picture was taken. Upon analyzing the image, the dimensions of each pixel were determined to be $187\ \mu m \times 187\ \mu m$, resulting in a field of view of $75\ mm \times 75\ mm$ after cropping.

Though the above method provides a satisfactory measure of the dimensions of each pixel, it does not accurately quantify the spatial resolution of the measurement system. In practice, the coupling of the lens, image intensifier and the camera leads to some level of inevitable "blurring" between pixels, effectively reducing the spatial resolution. Should a more refined estimate of spatial resolution be required, a resolution target could be used, which allows the user to determine the spacing required to fully resolve a pair of parallel lines when viewed through the full optical system.

3.6 Examination of Potential Sources of Error

Several potentials sources of error inherent to the measurement technique required consideration. These sources of error include: thermal blooming, photobleaching, attenuation, trapping and inertial effects. Several steps, which will now be described, were taken to quantify and minimize each source.

Thermal blooming refers to the heating of the dye (and water) due to constant laser irradiation and photobleaching refers to the decay of the fluorescence intensity also due to constant laser irradiation. Both these effects were minimized by scanning the laser beam with the rotating mirror. In the same facility, Lavertu

(2008) estimated that approximately 200 μs of constant laser irradiation resulted in a 2% decrease in fluorescence intensity. Using the same optical set-up as the current work, Perez-Alvarado (2016) estimated that the residence time of the laser beam in the volume represented by one pixel was 2 μs. It was therefore concluded that thermal blooming and photobleaching were negligible.

Attenuation occurs when the laser beam power decreases as it travels through dyed fluid (due to absorption of energy by the fluorescent dye). The end result is a loss in linearity between the fluorescence intensity and dye concentration. This effect was minimized by using dilute dye concentrations. Using the same optical set-up as the current work, Perez-Alvarado (2016) concluded negligible differences in fluorescence intensity when the laser was forced to travel an extra 10 cm through dyed fluid. The fact that the calibration curves were linear across the whole field of view further confirmed the lack of attenuation (see Figure 3.12).

Trapping refers to the absorption of the dye's emitted fluorescence by dye at another location. This was a possibility in the current work if dye located between the laser sheet and light detection system absorbed the fluorescence emitted by the dye as it crossed the laser sheet. Perez-Alvarado (2016) performed a test where he placed a glass tank between the calibration tank and the light detection system. The calibration tank was filled with dyed water and the glass tank was filled with either clean (baseline) or dyed water (to simulate a trapping scenario). The camera output for both configurations was compared and was found to have a negligible difference indicating that trapping effects were negligible.

Inertial, or buoyancy effects, were possible if large density differences existed between the dyed and un-dyed water or if large temperature gradients were present. The highest dye concentration used during experiments was $14\times 10^{-8}M$. This resulted in a density difference of 5×10^{-6} % between dyed and un-dyed water, assuming $\rho_{water} = 1\ kg/L$ and $MW_{dis.fluo.} = 376.3\ g/mol$. This was deemed

negligible. Temperature gradients were minimized by using water taken from the glass tank prior to each experiment. Temperature gradients due to heating from the laser were also minimized by the rapid scanning of the beam.

Chapter 4: Flow Validation, Experimental Conditions and Uncertainty Analysis

In the first section of this chapter, the procedure used to validate the flow and measurement technique will be described. The next section will then outline the experimental conditions and provide justifications for their selection. The final section will describe the statistical procedure used to quantify the uncertainty in the concentration measurements.

4.1 Flow Validation

To validate the turbulent jet structure and the measurement technique, concentration measurements of disodium fluorescein were obtained and compared to previous jet studies with similar experimental conditions. Since simple jets have been more thoroughly studied than coaxial jets, measurements were performed on a simple jet with a Reynolds number of 6700 at a downstream location of $x/D = 10$. Three works reporting scalar measurements (mass concentration or temperature) in a simple jet were used as benchmarks: Dahm and Dimotakis (1990), Mi *et al.* (2001) and Perez-Alvarado (2016). The radial profiles of the mean and root-mean-square (rms) of the concentration/temperature along with the centerline turbulence intensities were compared.

Dahm and Dimotakis used laser-induced fluorescence to perform concentration measurements of disodium fluorescein in a jet of water with $Re = 5000$. Measurements were taken along the jet centerline at downstream distances in the range: $0 < x/D < 350$. A noteworthy difference in their experimental conditions

was that their jet possessed a top-hat exit velocity profile, as opposed to a fully developed pipe flow exit velocity profile (present work). Mi *et al.* used cold-wire thermometry to obtain temperature measurements in a jet of air with Re =16000. They tested two different exit velocity profiles: top-hat and fully developed pipe flow. Radial measurements were obtained in the developing region, starting at $x/D = 8$ for the top-hat jet and $x/D = 15$ for the pipe flow jet. Both the measured scalar (temperature) and Reynolds number were notably different when compared to the present work. Finally, Perez-Alvarado used the same optical set-up as in the present work to make concentration measurements of disodium fluorescein in a jet of water with $Re = 10600$. His jet was produced by a constant area nozzle, and therefore had a fully developed pipe flow exit velocity profile. Radial measurements were obtained at a downstream distance of $x/D = 50$ and centerline measurements for $10 < x/D < 80$.

In Figure 4.1, the radial profile of the mean of the concentration obtained in the present work is plotted with the mean profile obtained by Mi *et al.* (2001) and Perez-Alvarado (2016). Note that Dahm and Dimotakis (1990) only recorded centerline concentration values, so their results are not included in Figure 4.1. The mean values of the concentration/temperature (C_{mean}) were normalized by their mean centerline $\left(C_{mean,CL}\right)$ values, and the radial distance (r) was normalized by the downstream distance (x). Very good agreement is observed between all three profiles, despite different downstream measurement locations and scalars measured (i.e., different Sc). This implies that the radial profile of the mean concentration had reached its self-similar state by $x/D = 10$.

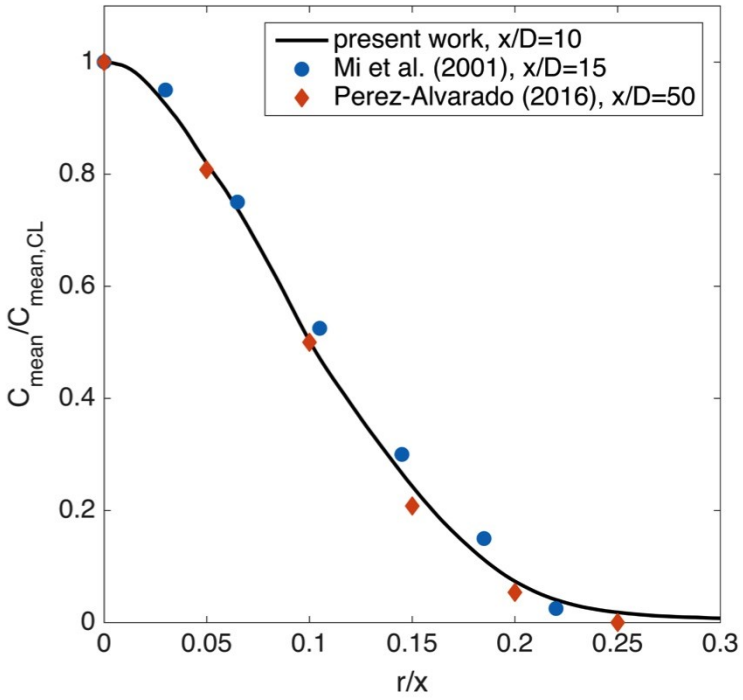

Figure 4.1: Radial profile of the mean of the concentration/temperature for the simple jet with $Re = 6700$ at $x/D = 10$ (fully developed pipe flow). Data of other authors included for comparison (– Present work; ● Mi et al. (2001), pipe flow, Re=16000, $x/D = 15$; ◆ Perez-Alvarado (2016), pipe flow, $Re = 10600$, $x/D = 50$).

In Figure 4.2, the radial profile of the rms of the concentration/temperature is plotted. Unlike the mean, the rms of the concentration had not reached self-similarity at $x/D = 10$. For this reason, an effort was made to only compare rms profiles at very similar downstream locations. Mi *et al.* (2001) were, therefore, the only authors whose results were plotted for comparison with the present work. The rms values of the concentration/temperature (c_{rms}) were normalized by their rms centerline $(c_{rms,CL})$ values and the radial distance (r) was normalized by the downstream distance (x).

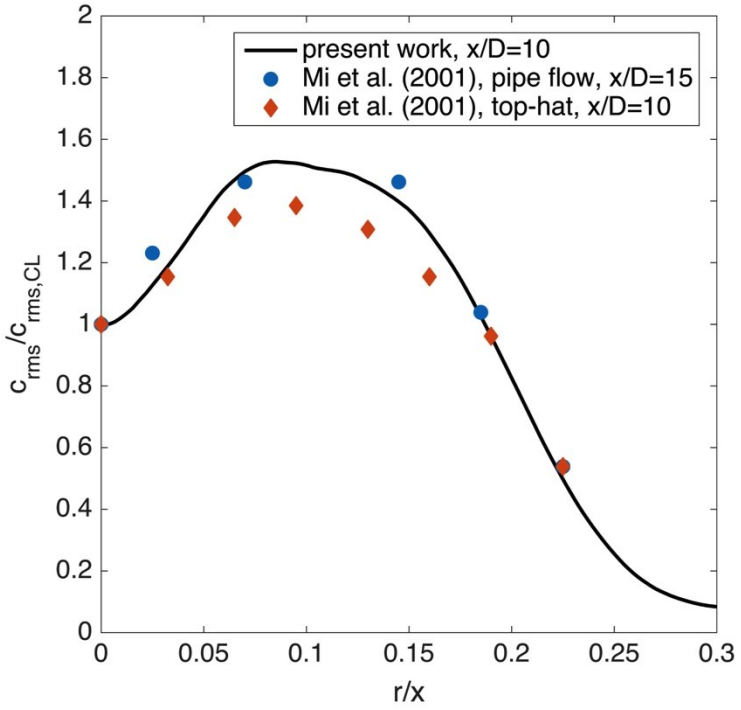

Figure 4.2: Radial profile of the rms of the concentration/temperature for the simple jet with $Re = 6700$ at $x/D = 10$ (fully developed pipe flow). Data of other authors included for comparison (– Present work; ● Mi et al. (2001), pipe flow, Re=16000, $x/D = 15$; ◆ Mi et al. (2001), top-hat, Re=16000, $x/D = 10$).

The present work is in good agreement with the results of Mi *et al.* (2001). This is especially true for the jet possessing a fully developed pipe flow exit velocity profile, as expected given the importance of initial conditions on the early flow development in jets (see Chapter 2). Significant deviations can be observed when comparing the present work to the jet with a top-hat exit velocity profile. Nevertheless, the agreement is good considering the differences in Sc, Re, and x/D between the two works.

The centerline concentration turbulence intensity obtained in the present and other works is listed in Table 4.1. Since the centerline turbulence intensity in the developing region has been shown to be a function of the Schmidt number, only past work with comparable Schmidt numbers was considered.

Table 4.1: Centerline concentration turbulence intensity for the simple jet. Data of other authors included for comparison.

Research project	**Experimental conditions**	$(c_{rms}/C_{mean})_{CL}$
Present work	pipe flow, $x/D = 10$, $Re = 6700$	0.070
Dahm and Dimotakis (1990)	top-hat, $x/D = 10$, $Re = 5000$	0.075
Perez-Alvarado (2016)	pipe flow, $x/D = 10$, $Re = 10600$	0.050

As can be observed in Table 4.1, the centerline concentration turbulence intensity in the present work is comparable to the value obtained by both Dahm and Dimotakis (1990) and Perez-Alvarado (2016). Differences between the present work and the work of Dahm and Dimotakis (1990) can be attributed to the differences in exit velocity profiles. Jets with a top-hat velocity exit profile have been shown to exhibit a faster rate of centerline turbulence intensity increase in the developing region than jets with a fully developed pipe flow exit velocity profile. The differences observed between the current work and the work of Perez-Alvarado (2016) presumably result from the difference in Reynolds number.

Overall the above results confirm the validity of the jet structure and measurement technique pertaining to the present work. Though a perfect match in experimental conditions was not possible, the general trends are in agreement with the benchmark papers.

4.2 Experimental Conditions

Coaxial jet experiments are characterized by several experimental conditions: the velocity ratio, Reynolds number of the inner and outer jets, the area ratio, and the nozzle exit velocity profile being the most important. In the current work, the selection of the experimental conditions was dictated by the project's objectives and practical applications, as well as the constraints imposed by the hydraulic set-up.

To facilitate the long-term objective of measuring differential diffusion effects, a velocity ratio of 1 was selected. The longer developing region associated with coaxial jets of $r_v = 1$ should provide a bigger domain for future measurements. Furthermore, the reduced shear between the inner and outer flows should theoretically make differential diffusion effects easier to isolate.

The inner jet had a Reynolds number of 6700 and the outer jet had a Reynolds number of 5500. These specific values were chosen by considering several factors. Firstly, any inner or outer Reynolds number exceeding approximately 8000 would cause the supply reservoirs to deplete before sufficient data was recorded. In addition, the increase in volumetric flow rate through the hydraulic set-up associated with these Reynolds numbers often resulted in bubbles being present in the coaxial jet (especially in the outer flow). Furthermore, Lavertu *et al.* (2008) demonstrated that differential diffusion effects were most significant at low Reynolds numbers. Turbulent flow at the nozzle exit was, however, an important requirement when considering the practical applications. For this reason, the inner jet Reynolds number was set at 6700, which, coupled with the requirement of $r_v = 1$, resulted in an outer jet Reynolds number of 5500.

The area ratio was 2.54 as this value was consistent with previous works and was relevant to the practical applications. Finally, the coaxial nozzle was assembled

using straight tubes, resulting in a fully developed pipe flow exit velocity profile. This nozzle geometry was selected instead of a converging nozzle geometry for ease of assembly and because the fully developed pipe flow exit velocity profiles have received less attention in previous coaxial jet studies.

To characterize the downstream development of the coaxial jet, planar concentration measurements were performed at three axial locations: $x/D_{in} = 2, 5$ and 10. In addition, three different jet configurations were tested at each axial location. The first configuration was that of a simple jet. This provided a benchmark against which coaxial jet measurements could be compared. In addition, scalar measurements in the developing region of simple jets have not been extensively performed. The second configuration was that of a coaxial jet with dye present only in the inner flow. The third configuration was that of a coaxial jet with dye present only in the outer flow. A schematic summarizing the downstream measurements locations, as well as a flow visualization for each jet configuration is presented in Figure 4.3.

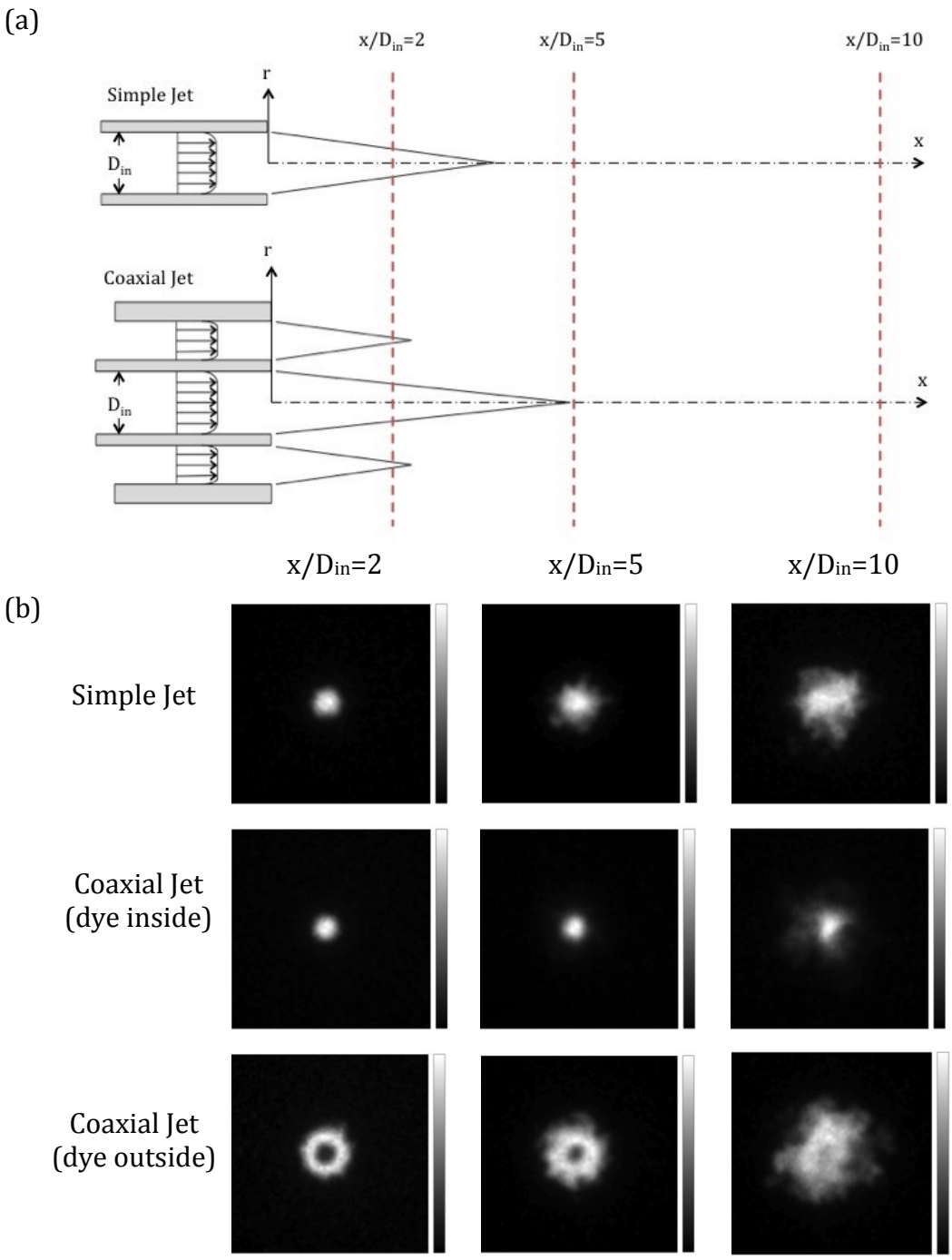

Figure 4.3: (a) Schematic of the developing region of the simple and coaxial jets. Measurement locations are marked by vertical, dashed lines (at $x/D_{in} = 2, x/D_{in} = 5$ and $x/D_{in} = 10$). (b) Instantaneous planar images at each measurement location for the three jet configurations (front view).

4.3 Uncertainty Analysis

To quantify the uncertainty in the concentration measurements, a statistical analysis of the results was performed. Several sources of error have already been considered in previous chapters. For example, in §3.4, inadvertently captured artifacts (such as the outline of the coaxial nozzle or glare from the computer) and electronic noise were accounted for during post-processing. In §3.5, uneven light sensitivity across the field of view was accounted for by performing a pixel-by-pixel calibration. Furthermore, steps were taken to minimize the effects of photobleaching, thermal blooming, trapping, attenuation and buoyancy. These sources of error are referred to as systematic errors and, as such, affect the measurements in a repeatable way. This section, however, is concerned with random errors, which affect the results in a random way and can be quantified through repeated measurements. Sources of random error include: vibrations, flow rate fluctuations, and sensor variability. Since the quantification of each source and the estimation of its effect on the final results (through error propagation) was not feasible, statistical methods were used.

As will be discussed in greater detail in Chapter 5, the final results of this work consisted (in part) of radial profiles of the mean, root-mean-square (rms) and skewness of the concentration. In the present work, two important sources of random error were considered: the variability between radial profiles (mean, rms and skewness) computed along different azimuthal directions (within the same experiment) and the variability between radial profiles obtained from different experiments.

The first source of error stems from the fact that a perfectly axisymmetric jet is an idealization that is not met in practice due to various factors, including: turbulent phenomena, vibrations, misalignments and irregularities in the coaxial nozzle. The subsequent analysis was performed to obtain an estimate of the true

radial profile and to quantify the uncertainty caused by jet asymmetries. To this end, radial profiles of the mean, rms and skewness of the concentration were plotted along 8 different azimuthal directions (at 45° increments) for each experiment. At every radial location, the mean (C_{mean}) and standard deviation (σ) of these profiles were calculated by way of the following formulas:

$$\mathsf{C}_{mean} = \frac{1}{N}\sum_{i=1}^{N} \mathsf{C}_i \tag{4.1}$$

$$\sigma = \sqrt{\frac{1}{N-1}\sum_{i=1}^{N} (\mathsf{C}_i - \mathsf{C}_{mean})^2}, \tag{4.2}$$

where N is the total number of radial profiles ($N = 8$) and C is the mean, rms or skewness of the concentration (depending on which statistical moment was considered). This yielded an estimate of the true value (C_{mean}) and an estimate of the uncertainty (σ) at every radial position, for each experiment. It is important to note that some of the error resulting from jet asymmetries was systematic in nature (tube irregularities and tube misalignments). Isolating the effects of these sources of error, however, was very difficult and, for this reason, the error was treated as random.

The second important source of random error stems from the fact that perfectly repeatable results are impossible due to random and unpredictable events (vibrations, unsteady flow, sensor fluctuations, etc.). To quantify the repeatability of the experimental set-up, the simple jet configuration was tested 3 times at $x/D_{in} = 10$, with measurement and experimental conditions identical to those described in §3.3 and §4.2. For each test, the radial profiles of the mean, rms and

skewness of the concentration were averaged along 8 azimuthal directions (as described above), yielding 3 independent profiles (one per test), for each statistical moment. At every radial position, the standard deviation (i.e., the uncertainty) was then computed using these 3 profiles.

Due to time constraints, repeated measurements were only performed on the simple jet configuration at $x/D_{in} = 10$. However, an estimate of the uncertainty related to repeatability needed to be determined for all other downstream locations and jet configurations. To this end, the largest uncertainty across all radial positions (within the jet structure) for the simple jet at $x/D_{in} = 10$ was selected as the most conservative choice.

The above procedure yielded two measures of uncertainty: uncertainty related to axial symmetry $(\sigma_{symmetry})$ and uncertainty related to repeatability (σ_{repeat}). These values were added in quadrature to obtain a total uncertainty value (σ_T), by way of the following formula:

$$\sigma_T = \sqrt{{\sigma_{symmetry}}^2 + {\sigma_{repeat}}^2}. \tag{4.3}$$

For the simple jet at x/D_{in}=10, the final radial profiles were obtained by averaging over the 8 azimuthal directions and then over the 3 repeatability tests. The error bars, which are shown in Figure 4.4 (a), represent $\pm\sigma_T$. For all other downstream locations and configurations, the profiles were only averaged over the 8 azimuthal directions, since there were no repeated measurements.

Figure 4.4 provides an example of the radial profiles of the mean, rms and skewness of the concentration plotted with the error bars for the simple jet configuration. The error bars are relatively small for the mean profiles (Figure 4.4

(a)) and become slightly larger for the rms profiles (Figure 4.4 (b)). The skewness, which represents a higher order statistical moment and is inherently slower to converge, possesses the largest uncertainty. This makes only qualitative conclusions possible when discussing the skewness of the concentration measurements. The radial profiles corresponding to other jet configurations are not shown, but possess an uncertainty that is comparable in magnitude. For clarity, the error bars are not shown on any plots in Chapter 5.

(a) (b) (c)

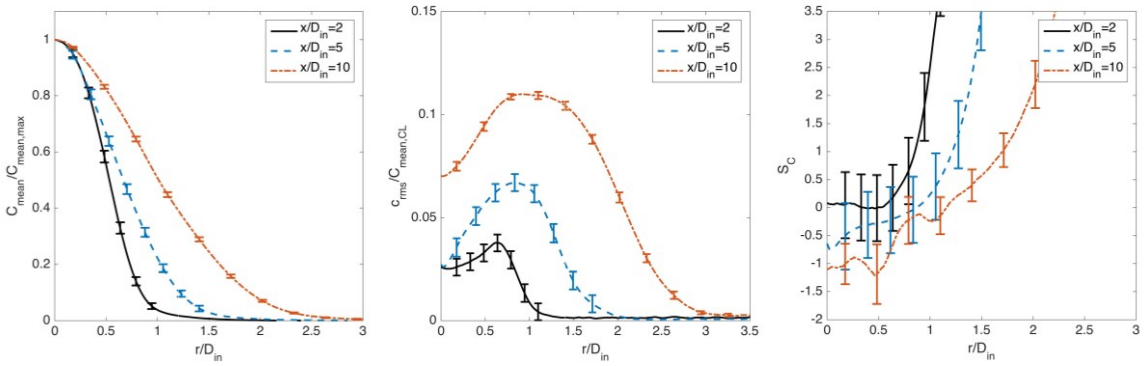

Figure 4.4: Radial profiles of the mean (a), rms (b) and skewness (c) of the concentration for the simple jet configuration. Error bars ($\pm\sigma_T$) are shown.

Chapter 5: Results and Discussion

In this chapter, the results of the statistics of the scalar field generated by both a simple and coaxial jet will be presented and discussed. The first section will consider the radial profiles of the mean, rms and skewness of the concentration, while the second section will consider the concentration probability density functions. In each section, the radial and downstream evolution of the jets will be discussed and the three different jet configurations described in §4.2 will be compared.

5.1 Radial Profiles of Statistical Moments

Radial profiles of the first three statistical moments (mean, rms and skewness) were computed at each downstream location ($x/D_{in} = 2, 5$ and 10) for the three jet configurations (simple jet, coaxial jet with dye present in the inner flow and coaxial jet with dye present in the outer flow). Each moment has a particular physical interpretation that can help quantify and understand the scalar mixing and early flow development.

5.1.1 Mean Profiles

The downstream evolution of the mean concentration profiles for the simple jet configuration ($Re = 6700$) is shown in Figure 5.1. In Figure 5.1 (a), the mean concentrations (C_{mean}) were normalized by the maximum mean concentration value of the profile $\left(C_{mean,max}\right)$ and the radial distance (r) was normalized by the

jet diameter (D_{in}). Figure 5.1 (b) depicts instantaneous photographs taken at each downstream location.

(a)

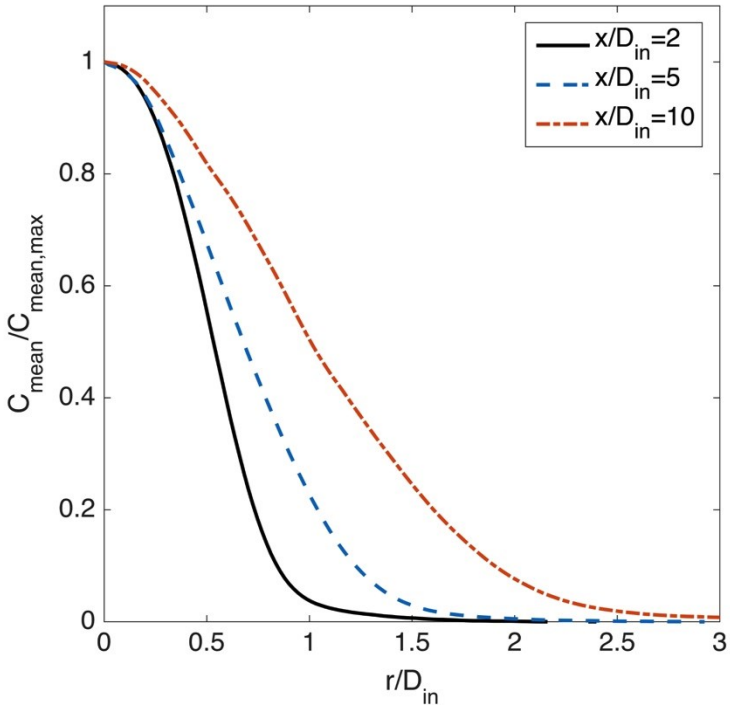

(b)

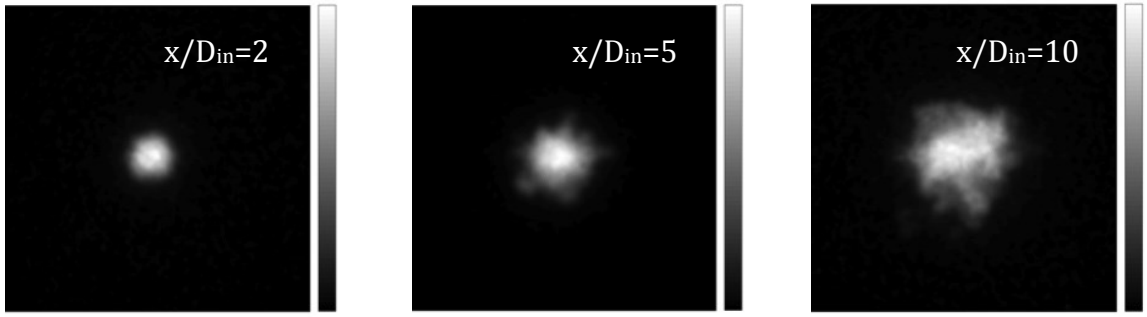

Figure 5.1: (a) Evolution of the mean concentration in the downstream direction for the simple jet ($Re = 6700$). (b) Instantaneous photographs.

It can be observed that, as the simple jet progresses downstream, the radial profiles of the mean concentration tend to increase in width and possess smaller mean concentration gradients $\left({}^{dC_{mean}}/_{dr}\right)$. These two trends are a product of the scalar mixing occurring at the jet boundary and within the jet structure. At the jet boundary, mixing between the jet fluid and the ambient fluid results in scalar transport in the radial direction and an overall increase in mean concentration profile width. Within the jet structure, the radial positions corresponding to the largest mean concentration gradients should theoretically also be the locations of highest scalar variance production (and mixing). The high levels of mixing have the effect of reducing concentration gradients, effectively flattening the mean concentration profile as the jet progresses downstream.

Figure 5.2 shows the downstream evolution of the radial profiles of mean concentration for the coaxial jet with dye present in the inner flow ($r_v = 1, Re_{in} = 6700$ and $Re_{out} = 5500$).

Similar to the simple jet, the mean concentration profile of the coaxial jet with dye present in the inner flow grows radially and becomes flatter in the downstream direction. Interestingly, the profiles at $x/D_{in} = 2$ and 5 are similar in shape (within the experimental error), indicating that the inner jet has not developed significantly in that interval, in contrast to the simple jet. To demonstrate the differences in radial spreading rate and downstream development between the two jet configurations, Figure 5.3 plots the concentration half-width $\left(r_{1/2}\right)$ as a function of downstream distance for both the simple jet and the coaxial jet with dye present in the inner flow.

(a)

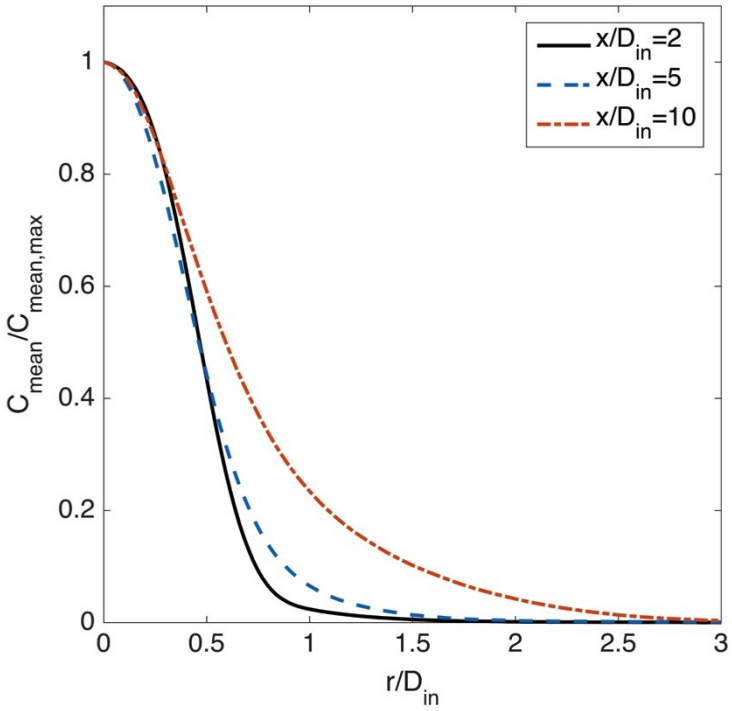

(b)

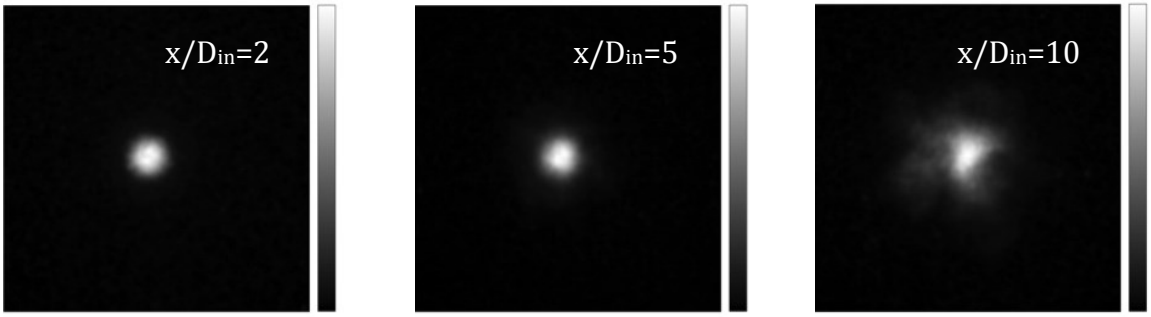

Figure 5.2: (a) Evolution of the mean concentration in the downstream direction for the coaxial jet with dye present in the inner flow ($r_v = 1, Re_{in} = 6700$ and $Re_{out} = 5500$). (b) Instantaneous photographs.

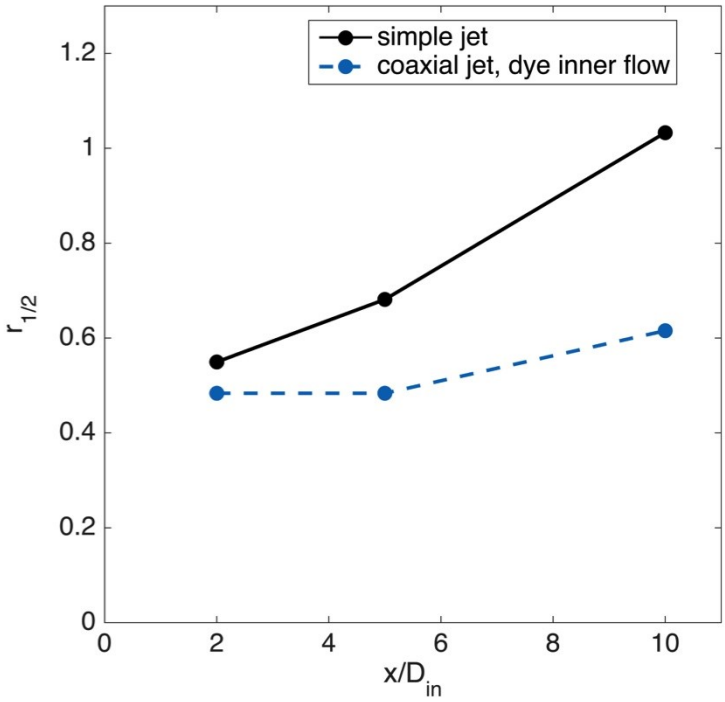

Figure 5.3: Concentration half-width $(r_{1/2})$ as a function of downstream distance, comparison between the simple jet and the coaxial jet with dye present in the inner flow.

At every downstream location considered, it can be observed that the simple jet has a larger half-width than the coaxial jet. In addition, the downstream evolution of the half-width reveals that the radial growth rate is also higher for the simple jet. These results imply that the simple jet develops at a faster rate than the inner jet of the coaxial jet. Similar comparisons and conclusions have been made in the past. Champagne and Wygnanski (1971) measured the length of the inner jet core as a function of the velocity ratio by way of velocity measurements in a coaxial jet of air. Longer inner cores are associated with longer developing regions and slower downstream jet development. They determined that the inner core was longest for $r_v = 1$ and decreased in length as the velocity ratio tended to 0 (i.e., a simple jet).

The simple jet's faster downstream development when compared to the coaxial jet can be attributed to differences in velocity gradients across the shear layers. In the simple jet configuration, the jet mixes with ambient fluid ($U_{ambient} = 0$) as it exits the nozzle, resulting in more significant velocity gradients than in the coaxial jet configuration, where mixing occurs between two flows of equal mean velocity (recall $r_v = 1$). This leads to more shear in the simple jet case, and as a result, more mixing and faster downstream development.

Figure 5.4 plots the mean concentration profiles for the coaxial jet with dye present in the outer flow ($r_v = 1, Re_{in} = 6700$ and $Re_{out} = 5500$). An off-axis mean concentration peak is observed for each profile, in addition to an increase in mean centerline concentration with downstream distance. These results are consistent with those of Cai *et al.* (2011), who used planar laser Rayleigh scattering to make ethylene concentration measurements in the outer flow of a coaxial jet. As their jet progressed downstream, from $x/D_{in} = 3.29$ to $x/D_{in} = 6.99$, the centerline concentration increased and the profiles became flatter as they approached their self-similar state.

(a)

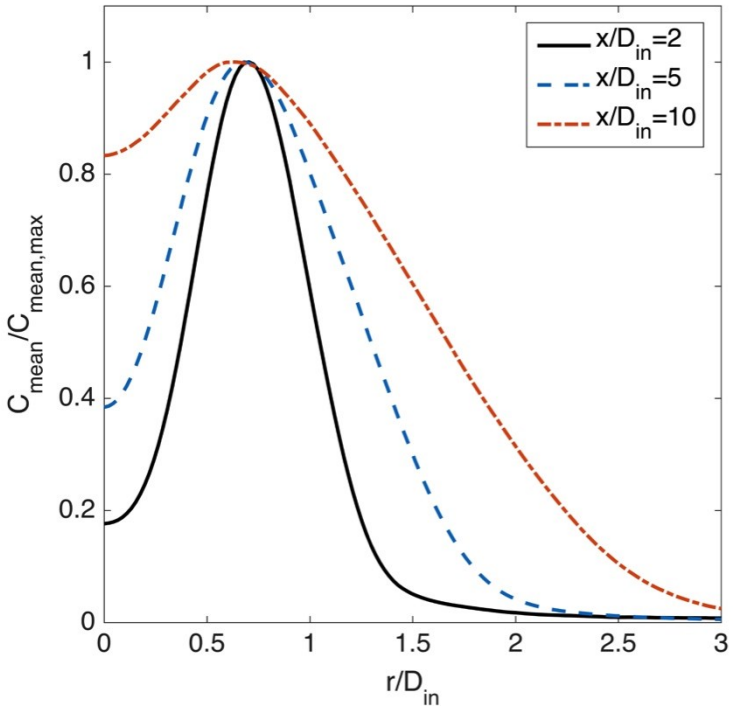

(b)

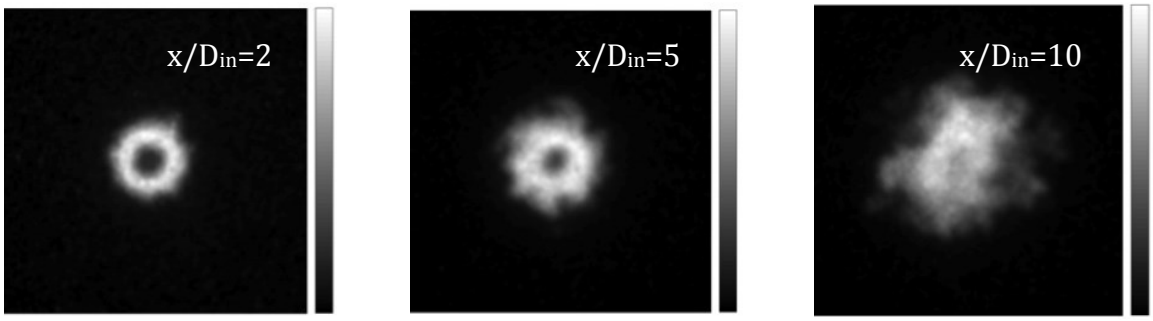

Figure 5.4: (a) Evolution of the mean concentration in the downstream direction for the coaxial jet with dye present in the outer flow ($r_v = 1, Re_{in} = 6700$ and $Re_{out} = 5500$). (b) Instantaneous photographs.

5.1.2 RMS Profiles

The rms of the concentration quantifies the magnitude of the concentration fluctuations at a given point in the jet structure. In the current context, high rms values are expected in regions where jet fluid and ambient fluid are actively mixing, but have not yet become fully mixed; and low rms values are expected in the jet core, in the ambient fluid or in regions where the jet and ambient fluid are well mixed and correlated,

Figure 5.5 plots the radial profiles of the rms of the concentration for the simple jet configuration. The rms values of the concentration (c_{rms}) were normalized by the centerline mean concentration $\left(C_{mean,CL}\right)$ and the radial distance (r) was normalized by the jet diameter (D_{in}).

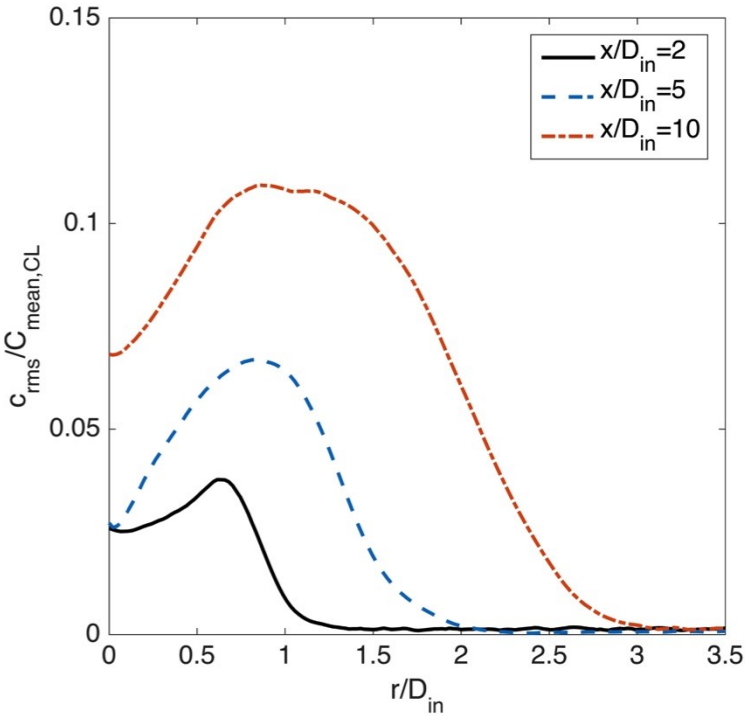

Figure 5.5: Evolution of the rms of the concentration in the downstream direction for the simple jet ($Re = 6700$).

Each profile has a local minimum in the rms of the concentration at the jet centerline and a maximum in the rms of the concentration at an off-axis radial position. Since large rms of the concentration values pertain to regions of active mixing between the jet core and ambient fluid, the maximum in the rms of the concentration marks the radial position corresponding to the center of the shear layer surrounding the jet core. It can also be observed that the radial position where the rms profiles peak corresponds closely to the radial position of maximum mean concentration gradient in Figure 5.1. This observation is consistent with the gradient-diffusion hypothesis (Pope, 2000). As the jet progresses downstream, the rms values (when normalized by the mean of the concentration) tend to increase in magnitude. The same trends were observed by Mi *et al.* (2001), who measured temperature in a simple jet of air, though differences in Schmidt/Prandtl numbers makes quantitative comparisons difficult.

Figure 5.6 plots the radial profiles of the rms of the concentration for the coaxial jet with dye present in the inner flow. When compared to the profiles in Figure 5.5, a noteworthy difference can be observed. At $x/D_{in} = 10$, the centerline rms concentration for the coaxial jet experiences a large increase, a trend not observed for the simple jet. To better illustrate this observation, Figure 5.7 plots the centerline concentration turbulence intensity $(c_{rms}/C_{mean})_{CL}$ as a functions of downstream distance for both the simple jet and coaxial jet with dye in the inner flow.

Figure 5.7 reveals that, while the centerline turbulence intensity of the two jets remains comparable until $x/D_{in} = 5$, the centerline turbulence intensity of the coaxial jet experiences a large increase at $x/D_{in} = 10$. Cai *et al.* (2011) also observed a large increase in centerline turbulence intensity between $x/D_{in} = 3$ and 10. This could, perhaps, be due to the entrainment of turbulent structures formed in the outer shear layer (between the outer jet and the ambient fluid) to the jet centerline. Ko and Kwan (1976) referred to these structures as secondary vortices, which they demonstrated to be important structures in the far

field for coaxial jet with $r_v \geq 0.7$. These secondary vortices would only be present in the coaxial jet configuration and, once entrained to the jet centerline, could act to increase concentration fluctuations. These structures could also be responsible for the more gradual decay in the rms of the concentration in the radial direction observed in Figure 5.6 (when compared to the simple jet).

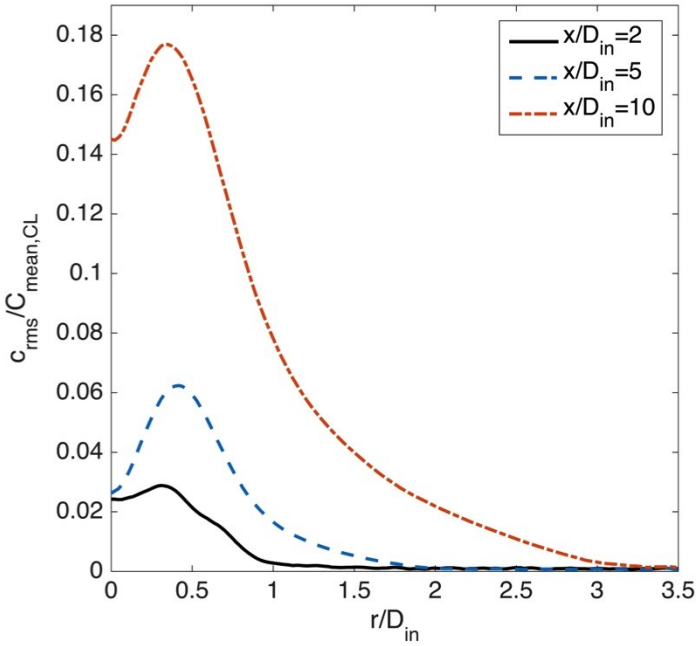

Figure 5.6: Evolution of the rms of the concentration in the downstream direction for the coaxial jet with dye present in the inner flow ($r_v = 1, Re_{in} = 6700$ and $Re_{out} = 5500$)

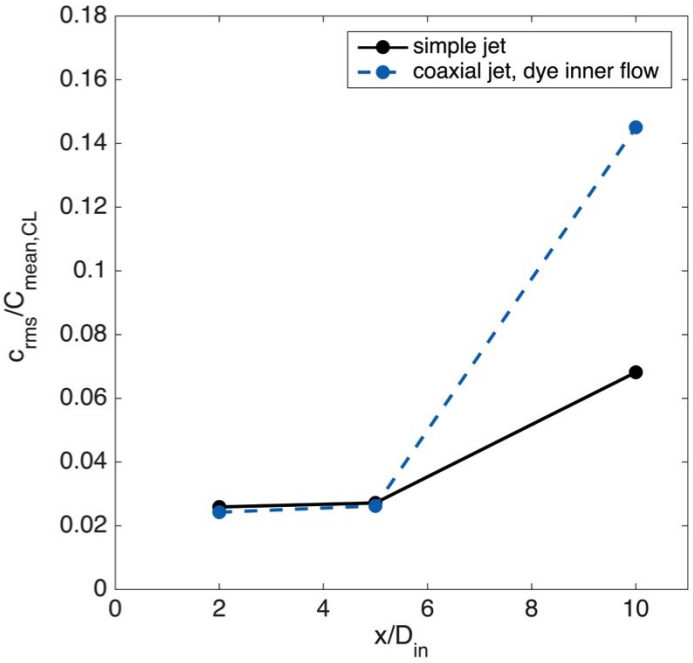

Figure 5.7: Centerline turbulence intensity as a function of downstream distance for the simple jet and the coaxial jet with dye present in the inner flow.

Figure 5.8 plots the radial profiles of the rms of the concentration for the coaxial jet with dye present in the outer flow. This configuration has the benefit of providing useful information about both the inner and outer shear layers simultaneously. This is because the outer jet (dyed) fluid mixes with both inner jet (un-dyed) fluid and the ambient (un-dyed) fluid, producing significant concentration fluctuations in both shear layers. As a result, the three curves in Figure 5.8 each possess many features that can be related to the shear layers (inner or outer) and/or the jet cores (inner or outer).

The rms profile at $x/D_{in} = 2$ has a local minimum at the centerline, corresponding to the inner jet core. The rms value then increases in the radial direction past an inflection point, towards an absolute maximum, corresponding to the center of the outer shear layer. In this profile, the center of the inner shear layer and the outer jet core are not resolved as distinct features, but are instead marked by an inflection point. This could possibly be an indication that the inner shear layer

has not yet developed by $x/D_{in} = 2$. The profile at $x/D_{in} = 5$ follows the same trends, with the exception that the center of the inner shear layer and the outer jet core are distinctly marked by a local maximum and minimum respectively, and not an inflection point. By $x/D_{in} = 10$, the extrema in the radial profiles have begun to flatten and merge, as the jet tends towards its self-similar state.

Villermaux and Rehab (2000), Cai *et al.* (2011) and Schumaker and Driscoll (2012) all presented scalar rms profiles in the developing region of a coaxial jet. Villermaux and Rehab (2000) plotted the rms profile of a coaxial jet of water at approximately $x/D_{in} = 1.25$. Their profile had a distinct maximum and minimum corresponding to the center of the inner shear layer and the outer jet core, rather than to an inflection point. This deviation could be due to the high velocity ratio used in their work ($r_v = 4$), leading to faster jet development. Cai *et al.* (2011) and Schumaker and Driscoll (2012) each reported rms profiles with shapes and trends similar to the current work. Direct comparisons, however, are difficult due to differences in experimental conditions and their importance on to the flow dynamics in the developing region.

The profiles presented in Figure 5.6 and Figure 5.8 are particularly useful in determining the radial positions within the coaxial jet structure where multi-scalar mixing effects (such as differential diffusion) could be significant, which was one of the objectives of the present work. The shear layers (marked by maxima in the profiles of the rms of the concentration) represent regions of active mixing between the inner and outer flows of the coaxial jet and between the outer flow and the ambient fluid. During a multi-scalar mixing process, a scalar would be present in each flow (and possibly in the ambient fluid as well), making the shear layers regions where at least 2 scalars are present simultaneously. These regions would therefore be of interest when measuring multi-scalar effects, such as differential diffusion.

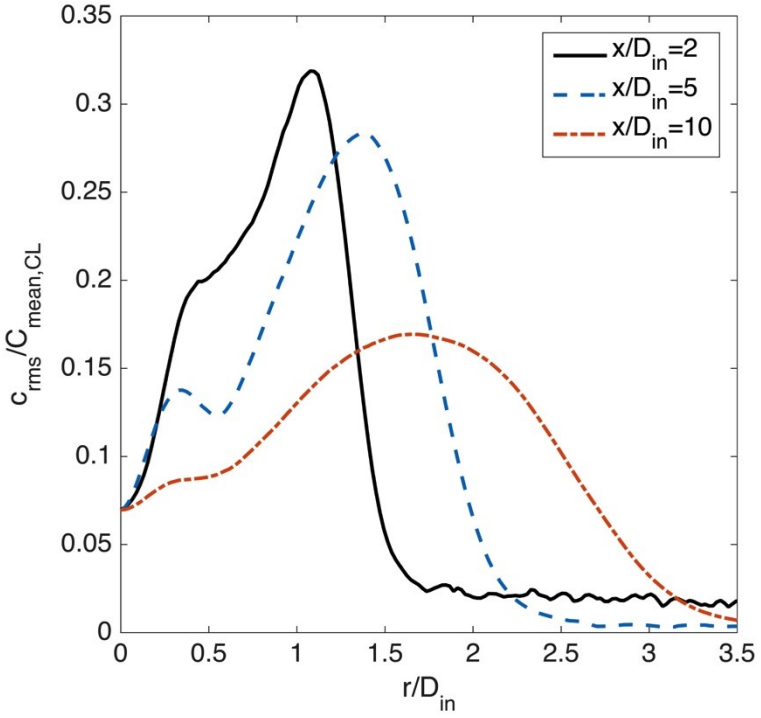

Figure 5.8: Evolution of the rms of the concentration in the downstream direction for the coaxial jet with dye in the outer flow ($r_v = 1, Re_{in} = 6700$ and $Re_{out} = 5500$).

5.1.3 Skewness Profiles

The radial profiles of the skewness of the concentration $\left(S_c = \frac{\langle C - C_{mean} \rangle^3}{{c_{rms}}^3}\right)$ presented in Figures 5.9, 5.10 and 5.11 provide additional insight on the concentration fluctuations. By definition, positive skewness indicates that, during a random process, values that are higher than the mean are more likely to occur than values that are smaller. Similarly, negative skewness indicates that smaller values are more likely. In the present context, positive skewness implies that pockets or lamellae of dyed fluid are being mixed in a background of un-dyed fluid and conversely for negative skewness. Recall that the large uncertainty in the measurements of the skewness of the concentration presented in §4.3 implies that only conclusions related to general trends can be confidently made in this section.

In Figure 5.9, the skewness profiles are plotted for the simple jet. At $x/D_{in} = 2$, the skewness is 0 at the jet centerline and remains constant until approximately $r/D_{in} = 0.5$, after which it becomes positive and increases with radial distance. The region of constant skewness corresponds to the inner core of the jet, where very little ambient fluid has been entrained. Concentration fluctuations are therefore symmetrically centered about the mean value, without a significant likelihood of large fluctuations in any direction. Once radial distances exceeding the inner core are reached, pockets of dyed jet fluid are mixed in a background of ambient fluid, resulting in positive skewness.

At $x/D_{in} = 5$ and 10, the skewness profiles are negative close to the jet centerline and then eventually become positive at some radial distance away from the centerline. The radial positions where S_c=0 correspond approximately to the radial positions where c_{rms} is maximized in Figure 5.5. The peaks in c_{rms} therefore represent a transition point from a mixing pattern where pockets of ambient fluid are being mixed in a background of core jet fluid to a mixing pattern where pockets of core jet fluid are being mixed in a background of ambient fluid. Mi *et al.* (2001) plotted the skewness profiles for a simple jet at farther downstream locations ($x/D_{in} > 25$), and also observed a transition from negative to positive skewness at radial positions corresponding to the peaks of their radial profile of rms of the concentration.

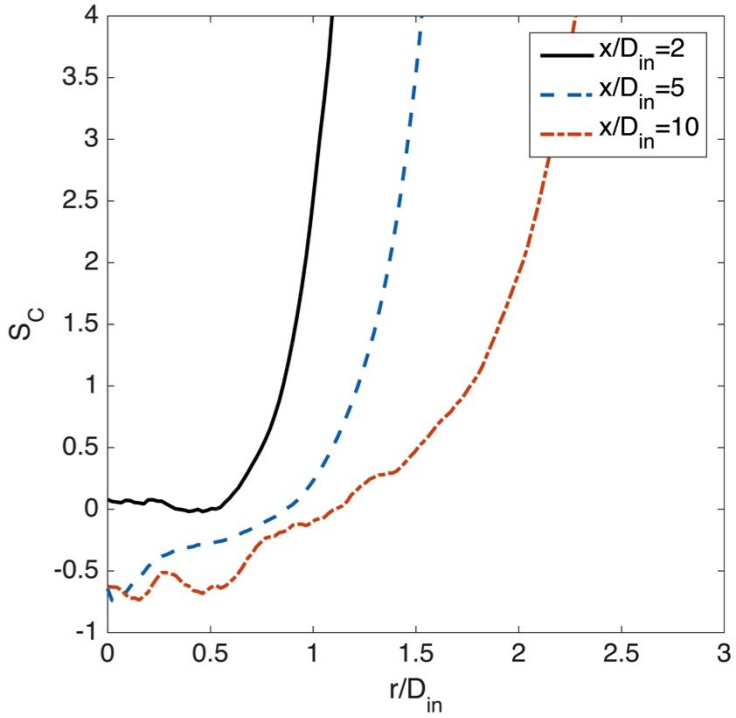

Figure 5.9: Evolution of the skewness of the concentration in the downstream direction for the simple jet ($Re = 6700$).

In Figure 5.10, the skewness profiles are plotted for the coaxial jet with dye present in the inner flow. The profile at $x/D_{in} = 2$ is very similar to the simple jet's profile both qualitatively and quantitatively (within experimental error), implying a similar jet structure. However, at $x/D_{in} = 5$ and 10, the shape of the profiles begins to deviate significantly. Notably, the transition from negative to positive skewness occurs at smaller radial distances for the coaxial jet. Perhaps the secondary vortices formed in the outer shear layer increase the probability of observing above average concentration values when they interact with pockets of inner jet fluid.

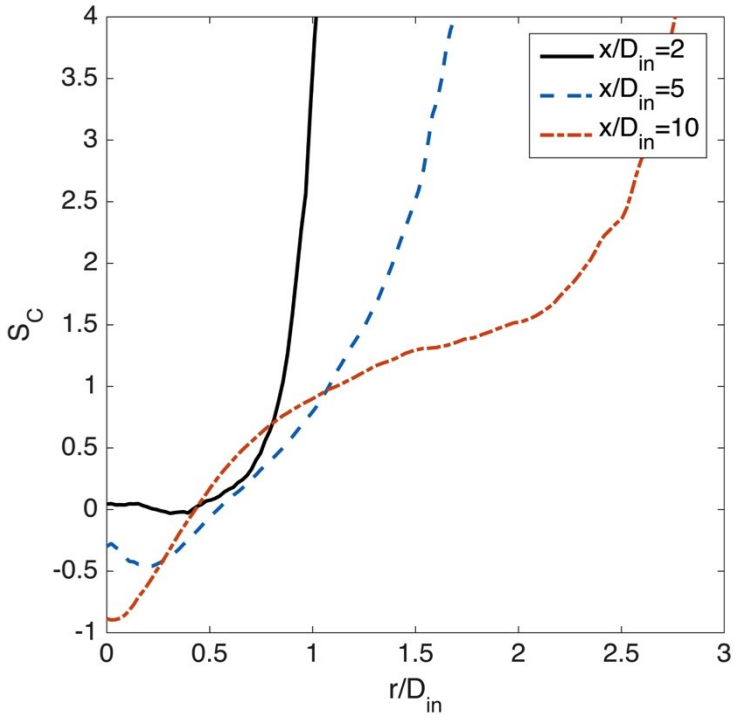

Figure 5.10: Evolution of the skewness of the concentration in the downstream direction for the coaxial jet with dye present in the inner flow ($r_v = 1, Re_{in} = 6700$ and $Re_{out} = 5500$).

Figure 5.11 plots the skewness profiles for the coaxial jet with dye present in the outer flow. Between the jet centerline and the inner shear layer (see Figure 5.8), the skewness is positive for all profiles, as pockets of dyed outer jet fluid are mixed in un-dyed inner jet fluid. Between the inner and outer shear layers, the skewness becomes negative, as pockets of un-dyed fluid from the inner jet and ambient fluid are now mixed in dyed outer jet fluid. Finally, at radial locations exceeding the outer shear layer, the profiles once again become positively skewed. To the author's knowledge, skewness profiles of scalar measurements have yet to be reported in coaxial jets.

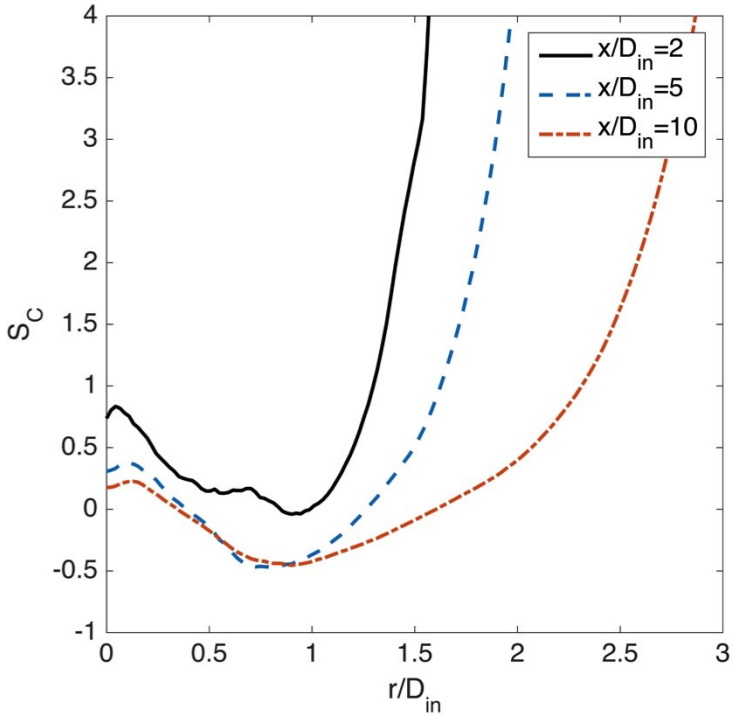

Figure 5.11: Evolution of the skewness of the concentration in the downstream direction for the coaxial jet with dye in the outer flow ($r_v = 1, Re_{in} = 6700$ and $Re_{out} = 5500$).

5.2 Probability Density Functions of Concentration Fluctuations

Probability density functions (PDFs) provide a full statistical description of the statistical moments of the concentration fluctuations at a point in the jet structure. They were computed at several radial and downstream locations for both the simple jet and the coaxial jet with dye present in the inner flow.

At each downstream location considered ($x/D_{in} = 2, 5$ and 10), PDFs were computed at 5 different radial positions $(r_0, r_{1/4}, r_{1/2}, r_{3/4}$ and $r_{9/10})$ extending from the jet centerline to the edge of the jet structure. These locations were selected by determining the radial positions at which the jet mean concentration had decayed

by a certain fraction of its centerline value; r_0 corresponds to the jet centerline, $r_{1/4}$ corresponds to the point where C has decayed by 25%, $r_{1/2}$ corresponds to the point where C has decayed by 50% (i.e., the jet half-width), $r_{3/4}$ corresponds to the point where C has decayed by 75% and finally, $r_{9/10}$ corresponds to the point where C has decayed by 90%.

Figure 5.12 depicts the PDFs for the simple jet and coaxial jet with dye present in the inner flow. The first column pertains to the simple jet and the second one to the coaxial jet. Each individual plot presents the PDF for one radial position at all three downstream locations. The instantaneous concentrations (C) were normalized by the local mean centerline value, and the vertical axis was plotted on a logarithmic scale (to highlight low probability events).

The PDFs pertaining to the simple jet will be discussed first. It can be observed that for all radial positions, the range of possible concentration values increases with downstream location. Mi *et al.* (2001) plotted centerline PDFs for their simple jet and also observed an increase in the range of measured concentration values with increasing downstream distance (for $x/D_{in} < 10$).

Referring to the sequence of plots in Figure 5.12 (a), (b), (c), (d) and (e), a trend from negative skewness to positive skewness with increasing radial distance can be observed. At $r = r_{1/2}$, the PDFs are nearly symmetric, as this radial position corresponds most closely to the center of the shear layer and marks the transition point between negative and positive skewness. Dahm and Dimotakis (1987) presented PDFs in the self-similar region at varying radial positions for their simple jet experiment. They also observed a transition from negative to positive skewness with an increase in radial position.

(a)

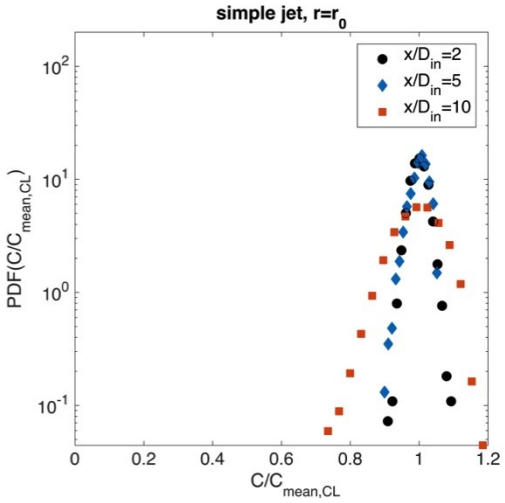
simple jet, r=r0
x/Din=2
x/Din=5
x/Din=10
PDF(C/Cmean,CL)
C/Cmean,CL

(f)

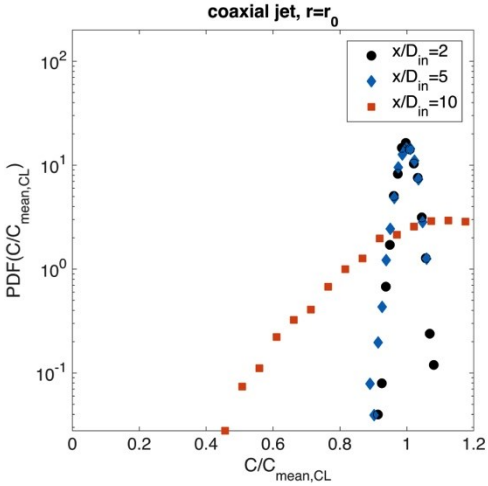
coaxial jet, r=r0
x/Din=2
x/Din=5
x/Din=10
PDF(C/Cmean,CL)
C/Cmean,CL

(b)

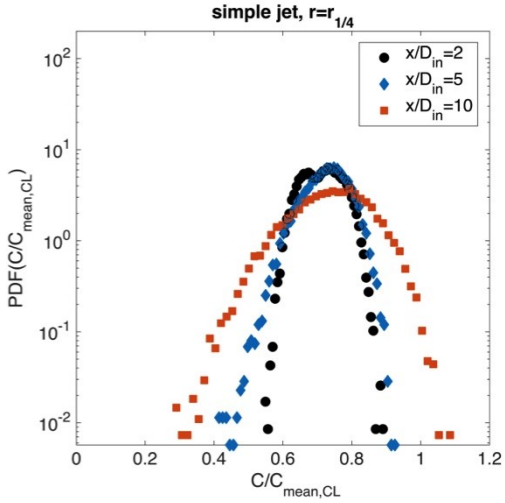
simple jet, r=r1/4
x/Din=2
x/Din=5
x/Din=10
PDF(C/Cmean,CL)
C/Cmean,CL

(g)

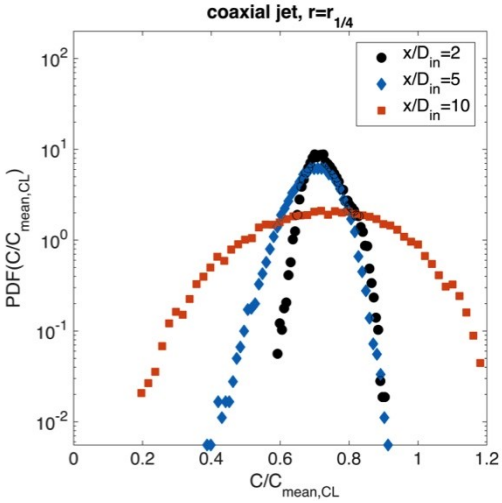
coaxial jet, r=r1/4
x/Din=2
x/Din=5
x/Din=10
PDF(C/Cmean,CL)
C/Cmean,CL

(c)

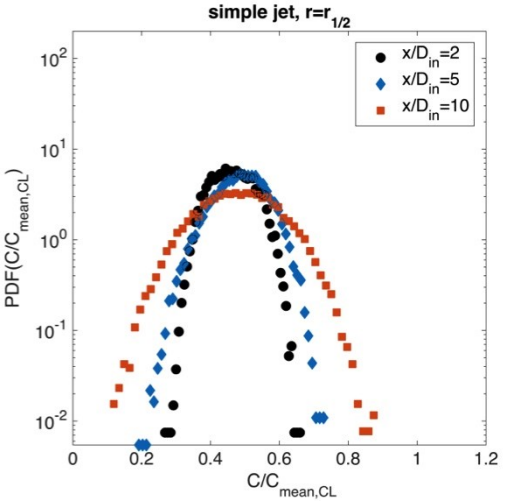
simple jet, r=r1/2
x/Din=2
x/Din=5
x/Din=10
PDF(C/Cmean,CL)
C/Cmean,CL

(h)

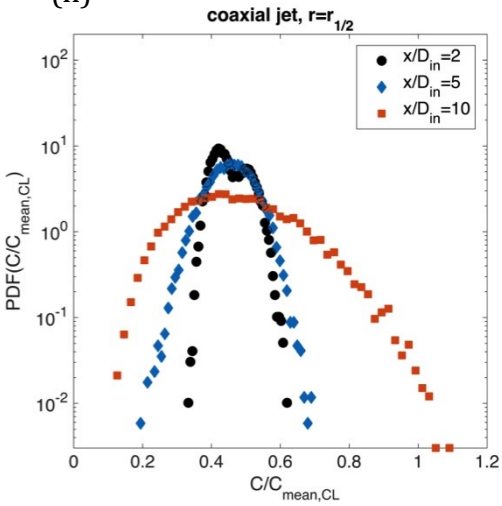
coaxial jet, r=r1/2
x/Din=2
x/Din=5
x/Din=10
PDF(C/Cmean,CL)
C/Cmean,CL

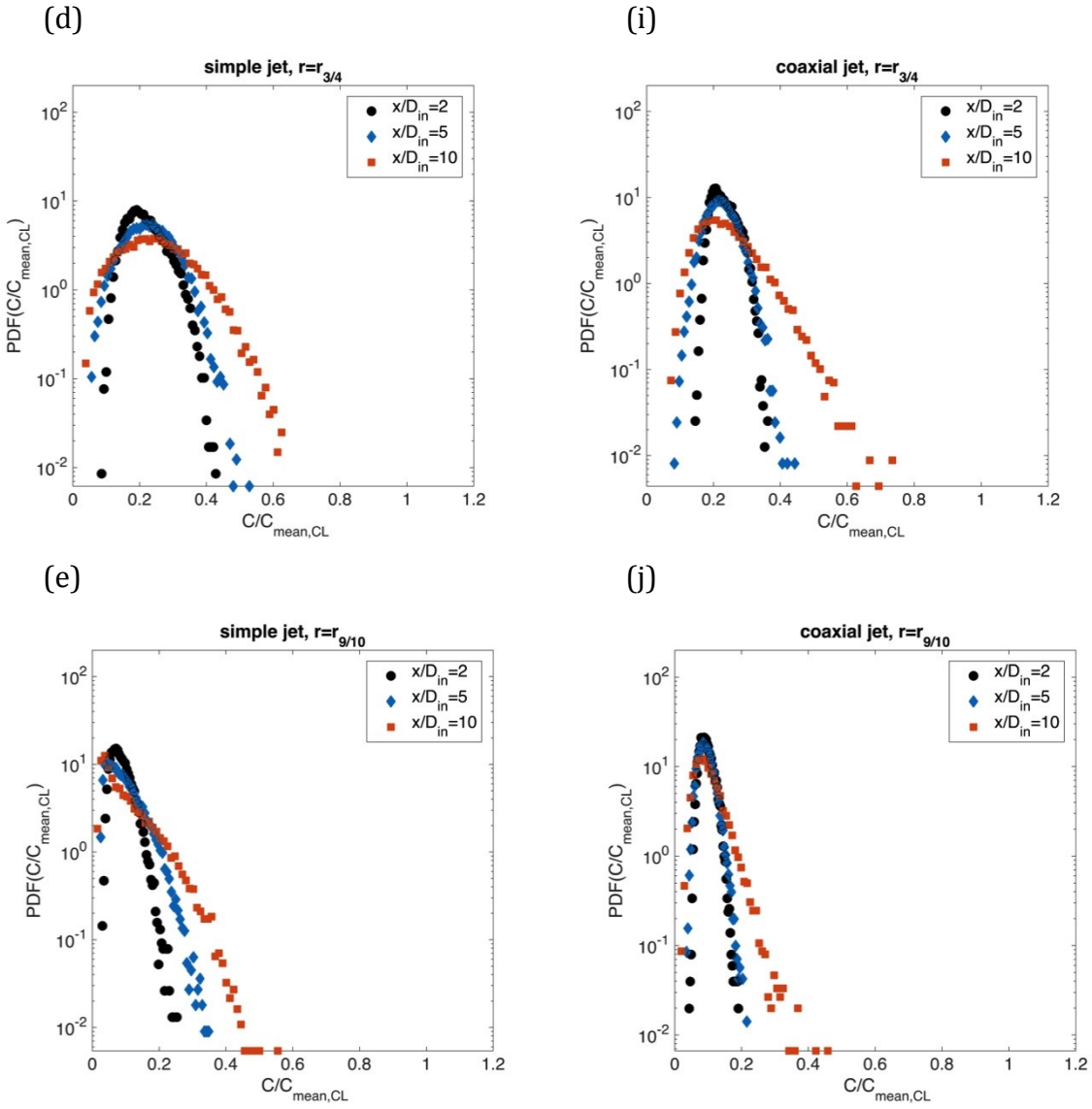

Figure 5.12: Radial and downstream evolution of the probability density functions for both the simple jet (a, b, c, d, e) and the coaxial jet with dye in the inner flow (f, g, h, i, j).

When comparing the PDFs computed for the simple jet to those computed for the coaxial jet with dye present in the inner flow, the same trend in concentration rms and skewness emerge. Nevertheless, a noteworthy difference is observed in Figure 5.12 (f), where the PDF at $x/D_{in} = 10$ has a much different shape than its simple jet counterpart in Figure 5.12 (a). While both PDFs are negatively skewed,

the coaxial jet PDF implies a much higher likelihood of observing low concentration fluid. This could, once again, be a result of the secondary vortices formed in the outer shear layer, which act to entrain pockets of un-dyed fluid to the jet centerline.

Villermaux and Rehab (2000) measured centerline PDFs in the developing region of a coaxial jet with $r_v = 4$. Interestingly, the PDF computed at $x/D_{in} = 1.25$ was bimodal in shape, implying the presence of unmixed dyed and un-dyed fluid. The authors then observed that the two peaks merged into one as the flow progressed downstream. In the present work, this was not observed, perhaps because measurements were not performed close enough to the nozzle exit. Their PDFs, however, were asymmetric ($S_c \neq 0$) for all downstream distances considered, while in the current work, the PDF at $x/D_{in} = 2$ was nearly symmetric ($S_c \approx 0$). Symmetric concentration fluctuations are expected in the inner core, where only core fluid is present. The lack of symmetry observed in Villermaux and Rehab's PDFs could be a result of increased fluid entrainment due to the high velocity ratio employed in their experiment.

Chapter 6: Conclusions

6.1 Thesis Review and Recommendations for Future Work

This thesis served to investigate the scalar mixing process in the developing region of a turbulent coaxial jet. Planar scalar measurements were obtained at 3 downstream locations ($x/D_{in} = 2, 5$ and 10) for a coaxial jet with: $Re_{in} = 6700$, $Re_{out} = 5500, Sc = 2000, A_{o/i} = 2.54, r_v = 1$ and a fully developed pipe flow exit velocity profile. Planar scalar measurements were also obtained at the same downstream locations for a simple jet with $Re = 6700$.The results and main observations of this work will now be summarized.

The radial profiles of the mean of the concentration for both the simple and coaxial jets displayed an overall increase in width and decrease in mean concentration gradient $\left({}^{dC_{mean}}/_{dr}\right)$ with downstream distance. When comparing the evolution of the jet half-width in the downstream direction between the simple jet and the coaxial jet (with dye in the inner flow), the simple jet was consistently wider and displayed a larger radial growth rate. This was related to more significant shear present between the simple jet and the ambient fluid when compared to the coaxial jet, where inner jet fluid mixes with outer jet fluid moving at the same mean velocity.

The radial profiles of the root-mean-square (rms) of the concentration revealed that both simple and coaxial jets possessed a peak in concentration rms corresponding to the location(s) of the shear layers describes in §2.2. When considering the centerline concentration turbulence intensity $(c_{rms}/C_{mean})_{CL}$, the

coaxial jet displayed a significant increase in value at $x/D_{in} = 10$ when compared to the simple jet. This was related to secondary turbulent structures formed in the outer shear layer of the coaxial jet, which served to increase concentration fluctuation when entrained to the jet centerline.

The radial profiles of the skewness of the concentration and the probability density functions provided additional statistical insight on the concentration fluctuations. Most notably, it was observed that both the simple and coaxial jets (with dye in the inner flow) possessed negative skewness at the jet centerline, whose value would then increase an eventually become positive with increasing radial distance. This was related to the fact that near the jet centerline (for both configurations) pockets of un-dyed fluid were being mixed with a background of dyed fluid. As the radial distance increased and the shear layer was crossed, this mixing pattern shifted towards one where pockets of dyed fluid were being mixed with a background of un-dyed fluid.

The motivation behind the present work was both fundamental and practical in nature. Fundamentally, coaxial jets represent a relatively simple shear flow, which makes them interesting to study from an academic standpoint. Practically, coaxial jets are found in fuel injectors, in the exhaust of high-bypass jet engines, as well as in many other applications. While the results obtained in this work provided insight on various aspects of the scalar mixing process, three noteworthy points of discussion deserve elaboration.

Firstly, the results provided useful information pertaining the inner and outer shear layers of the coaxial jet. In particular, regions of active mixing between the inner and outer flows, and between the outer flow and the ambient fluid were associated with high root-mean-square (rms) of the concentration values. During a multi-scalar mixing process in a coaxial jet, these would be the regions of active mixing between both scalars, as opposed to the jet cores, where only one scalar is

present. The shear layers, therefore, are most likely the best measurement locations for quantifying multi-scalar effects, such as differential diffusion.

Secondly, the results supported the fact that higher mean velocity gradients lead to more mixing and faster jet development. This represents a trend that can be leveraged to reduce combustion chamber size in fuel injector applications. In fact, other sources of mean velocity shear, such as swirl, are often introduced in these devices to enhance mixing.

Lastly, the results imply the presence of secondary vortices (formed in the outer shear layer of the coaxial jet) at the jet centerline, at $x/D_{in} = 10$. Understanding these structures and how they develop could help optimize the design of jet engines.

This work also represents an initial set of measurements to be used as a reference in future projects. Several recommendations, which could be undertaken to advance this work, are proposed.

Firstly, spectral analysis of the concentration fluctuations would provide much information related to the coherent structures formed in the shear layers and could help confirm the presence of secondary vortices.

Secondly, investigating the effect of mean velocity gradients by systematically varying the velocity ratio and/or the Reynolds number would be a useful undertaking. Since fuel injectors usually operate at high velocity ratios to enhance mixing, experiments in this regime would also be particularly relevant.

Lastly, performing simultaneous measurements of two scalars in a coaxial jet remains the ultimate goal of this research. Quantifying differential diffusion effects in a coaxial jet would be useful for combustion applications.

6.2 Contributions of the Present Study

As a final point of discussion, the novel contributions made by this thesis to the body of knowledge relating to turbulent jets will now listed.

This thesis provides the first set of planar scalar measurements in a simple jet obtained at downstream distances of $x/D_{in} < 5$. Dahm and Dimotakis (1990) only performed centerline measurements and Mi *et al.* (2001) only reported radial profiles at downstream distances larger than $x/D_{in} = 8$ (thought they presented PDFs as close as $x/D_{in} = 2$).

The experimental conditions used when performing tests on the coaxial jet were entirely novel in the literature. In addition, radial profiles of the skewness of the concentration in coaxial jets have never been presented (for any experimental conditions).

In conclusion, the present work serves to build on previous studies investigating scalar mixing in turbulent jets, while also providing new insight on the mixing that occurs in the developing region. In addition, the results represent a benchmark for future studies, which will hopefully be undertaken to help further our understanding of scalar mixing in turbulent flows.

References

BALL, CG., FELLOUAH, H. AND POLLARD, A. 2012 The flow field in turbulent round free jets. *Progress in Aerospace Sciences* **50**, 1–26.

BECKER, H., HOTTEL, H. AND WILLIAMS, G. 1967 The nozzle-fluid concentration field of the round, turbulent, free jet. *Journal of Fluid Mechanics* **30**, 285.

BREIDENTHAL, R. 1981 Structure in turbulent mixing layers and wakes using a chemical reaction. *Journal of Fluid Mechanics* **109,** 1-24.

BUCH, KA. AND DAHM, W. 1996 Experimental study of the fine-scale structure of conserved scalar mixing in turbulent shear flows. Part 1. Sc>>1. *Journal of Fluid Mechanics* **317**, 21-71.

CABRA, R., CHEN, JY., DIBBLE, RW., KARPETIS, AN. AND BARLOW, RS. 2005 Lifted methane–air jet flames in a vitiated coflow. *Combustion and Flame* **143,** 491–506.

CAI, J., DINGER, M., LI, W., CARTER, C., RYAN, M. AND TONG, C. 2011 Experimental study of three-scalar mixing in a turbulent coaxial jet. *Journal of Fluid Mechanics* **685**, 495–531.

CHAMPAGNE, FH. AND WYGNANSKI, IJ. 1971 An experimental investigation of coaxial turbulent jets. *International Journal of Heat and Mass Transfer* **14**, 1445-1464.

DAHM, W. 1985 Experiments on entrainment, mixing, and chemical reactions in turbulent jets at high Schmidt number. Ph.D. thesis, California Institute of Technology.

DAHM, W. AND DIMOTAKIS, P. 1987 Measurements of entrainment and mixing in turbulent jets. *AIAA journal.* **25**, 1216-1223.

DAHM, W. AND DIMOTAKIS, P. 1990 Mixing at large Schmidt number in the self-similar far field of turbulent jets. *Journal of Fluid Mechanics* **217**, 299–330.

DAHM, W., FRIELER, CE. AND TRYGGVASON, G. 1992 Vortex structure and dynamics in the near field of a coaxial jet. *Journal of Fluid Mechanics* **241**, 371–402.

DIMOTAKIS, PE. 2000 The mixing transition in turbulent flows. *Journal of Fluid Mechanics* **409**, 69-68.

Dewey, CF. 1976 Qualitative and quantitative flow field visualization utilizing laser-induced fluorescence. *AGARD Conf. Froc*. 193.

DOWLING, D. AND DIMOTAKIS, P. 1990 Similarity of the concentration field of gas-phase turbulent jets. *Journal of Fluid Mechanics* **218**, 109.

DYER, MJ. AND CROSLEY, DR. 1982 Two-dimensional imaging of OH laser-induced fluorescence in a flame. *Optics Letters* **7,** 382-384.

FELLOUAH, H., BALL, C.G. AND POLLARD, A. 2009 Reynolds number effects within the development region of a turbulent round free jet. *International Journal of Heat and Mass Transfer* **52**, 3943–3954.

GASKIN, S. 1995 Single Buoyant Jets in a Crossflow and the Advected Line Thermal. PhD thesis, University of Canterbury.

GASKIN, S. AND WOOD, IR. 2001 Flow structure and mixing dynamics of the advected line thermal. *Journal of Hydraulic Research* **39:5**, 459-468.

Guilbault, GG. 1973 *Practical fluorescence: Theory, methods, and techniques.* Marcel Dekker, INC.

GUILLARD, F., FRITZON, R., REVSTEDT, J., TRÄGÅRDH, C., ALDÉN, M., AND FUCHS, L. 1998 Mixing in a confined turbulent impinging jet using planar laser-induced fluorescence. *Experiments in Fluids* **25**, 143–150.

HUSSEIN, H., CAPP, S. AND GEORGE, W. 1994 Velocity measurements in a high-Reynolds-number, momentum-conserving, axisymmetric, turbulent jet. *Journal of Fluid Mechanics* **258**, -1, 31–75.

KO, N. AND AU, H. 1981 Initial region of subsonic coaxial jets of high mean-velocity ratio. *Journal of Fluids Engineering* **103,** 335-338.

KO, N. AND DAVIES, P. 1971 The near field within the potential cone of subsonic cold jets. *Journal of Fluid Mechanics* **50**, 49–78.

KO, N. AND KWAN, A. 1976 The initial region of subsonic coaxial jets. *Journal of Fluid Mechanics.* **73**, 305.

KOLMOGOROV, AN. 1941 (a) Dissipation of energy in the locally isotropic turbulence. *Dokl. Akad. Nauk. SSSR* **32**, 16-18.

KOLMOGOROV, AN. 1941 (b) The local structure of turbulence in incompressible viscous fluid for very large Reynolds numbers. *Dokl. Akad. Nauk. SSSR* **30**, 301-305.

KOLMOGOROV, AN. 1941 (c) On generation of isotropic turbulence in an incompressible viscous liquid. *Dokl. Akad. Nauk. SSSR* **31**, 538-540.

KOOCHESFAHANI, MM. 1984 Experiments on turbulent mixing and chemical reactions in a liquid mixing layer. PhD thesis, California Institute of Technology.

KYCHAKOFF, G., HOWE., RD. AND HANSON, RK. 1982 Quantitative visualization of combustion species in a plane. *Applied optics* **21**, 3225-3227.

LAVERTU, TM. 2008 Differential diffusion in a turbulent jet. PhD thesis, McGill University.

LAVERTU, TM., MYDLARSKI, L., AND GASKIN, S. 2008 Differential diffusion of high-Schmidt-number passive scalars in a turbulent jet. *Journal of Fluid Mechanics* **612**, 439–475.

LI, W., YUAN, M., CARTER, C., AND TONG, C. 2017. Experimental investigation of the effects of mean shear and scalar initial length scale on three-scalar mixing in turbulent coaxial jets. *Journal of Fluid Mechanics* **817**, 183–216.

MI, J., NOBES, DS. AND NATHAN, GJ. 2001 Influence of jet exit conditions on the passive scalar field of an axisymmetric free jet. *Journal of Fluid Mechanics* **432**, 91-125**.**

MILLER, PL. AND DIMOTAKIS, PE. 1991 Reynolds number dependence of scalar fluctuations in a high Schmidt number turbulent jet. *Physics of Fluids A* **3**, 1156-1163.

OWEN, FK. 1976 Simultaneous laser measurements of instantaneous velocity and concentration in turbulent mixing. *AGARD Conf. Proc*. 193.

PANCHAPAKESAN, N. AND LUMLEY, J. 1993 Turbulence measurements in axisymmetric jets of air and helium. Part 1. Air jet. *Journal of Fluid Mechanics* **246**, 197-223.

PANCHAPAKESAN, N. AND LUMLEY, J. 1993 Turbulence measurements in axisymmetric jets of air and helium. Part 2. Helium jet. *Journal of Fluid Mechanics* **246**, 225-247.

PEREZ-ALVARADO, A. 2016 Effect of background turbulence on the scalar field of a turbulent jet. PhD thesis, McGill University.

PEREZ-ALVARADO, A., MYDLARSKI, L. AND GASKIN, S. 2016 Effect of the driving algorithm on the turbulence generated by a random jet array. *Exp. Fluids* 57:20.

POPE, SB. 2000 *Turbulent Flows.* Cambridge University Press.

READY, JF. 1978 *Industrial Applications of Laser.* Academic Press.

REHAB, H. AND VILLERMAUX, E. 1997 Flow regimes of large-velocity-ratio coaxial jets. *Journal of Fluid Mechanics* **345**, 357-381.

RIBEIRO, MM. AND WHITELAW, JH. 1976 Turbulent mixing of coaxial jets with particular reference to the near-exit region. *Journal of Fluids Engineering*. **98**, 285-291.

ROWINSKI, D. AND POPE, SB. 2013 An investigation of mixing in a three-stream turbulent jet. *Physics of Fluids* **25**, No. 10, 105105.

SAYLOR, JR. 1995 Photobleaching of disodium fluorescein in water. *Experiments in Fluids* **18**, 445–447.

SAYLOR, JR. AND SREENIVASAN, KR. 1998 Differential diffusion in low Reynolds number water jets. *Physics of Fluids* **10** No. 5, 1135-1146.

SCHUMAKER, S. 2009. An experimental investigation of reacting and nonreacting coaxial jet mixing in a laboratory rocket engine. PhD thesis, University of Michigan.

SCHUMAKER, SA. AND DRISCOLL, JF. 2012 Mixing properties of coaxial jets with large velocity ratios and large inverse density ratios. *Physics of Fluids* **24**, 055101-1

TENNEKES, H. AND LUMLEY, JL. 1972 *A First Course in Turbulence.* The MIT Press.

VANDERWEL, C. AND TAVOULARIS, S. 2014 On the accuracy of PLIF measurements in slender plumes. *Experiments in Fluids* **55**, 8.

VILLERMAUX, E. AND REHAB, H. 2000. Mixing in coaxial jets. *Journal of Fluid Mechanics* **425**, 161-185.

VLIET, E., BERGEN, S., DERKSEN, J., PORTELA, L. AND AKKER, H. 2004 Time-resolved, 3D, laser-induced fluorescence measurements of fine-structure passive scalar mixing in a tubular reactor. *Experiments in Fluids* **37**, 1–21.

WALKER, DA. 1987 A fluorescence technique for measurement of concentration in mixing liquids. *J. Phys. E: Sci. Instrum*. **20**, 217-224.

WANG, G. AND FIEDLER, H. 2000 On high spatial resolution scalar measurement with LIF. *Experiments in Fluids* **29**, 265–274.

WANG, G. AND FIEDLER, H. 2000 On high spatial resolution scalar measurement with LIF. *Experiments in Fluids* **29**, 257–264.

WILSON, RAM. AND DANCKWERTS, PV. 1964 Studies in turbulent mixing—II A hot-air jet. *Chemical Engineering Science.* **19**, 885–895.

WYGNANSKI, I. AND FIEDLER, H. 1969 Some measurements in the self-preserving jet. *Journal of Fluid Mechanics* **38,** 577–612.

XU, G. AND ANTONIA, R. 2002 Effect of different initial conditions on a turbulent round free jet. *Experiments in Fluids.* **33,** 677–683.